UNVEILING MOLECULAR SECRETS: AN LLM-AUGMENTED LINEAR MODEL FOR EXPLAINABLE AND CALIBRATABLE MOLECULAR PROPERTY PREDICTION

Anonymous authors
Paper under double-blind review

ABSTRACT

Explainable molecular property prediction is essential for various scientific fields, such as drug discovery and material science. Despite delivering intrinsic explainability, linear models struggle with capturing complex, non-linear patterns. Large language models (LLMs), on the other hand, yield accurate predictions through powerful inference capabilities yet fail to provide chemically meaningful explanations for their predictions. This work proposes a novel framework, called *MoleX*, which leverages LLM knowledge to build a simple yet powerful linear model for accurate molecular property prediction with faithful explanations. The core of *MoleX* is to model complicated molecular structure-property relationships using a simple linear model, augmented by LLM knowledge and a crafted calibration strategy. Specifically, to extract the maximum amount of task-relevant knowledge from LLM embeddings, we employ information bottleneck-inspired fine-tuning and sparsity-inducing dimensionality reduction. These informative embeddings are then used to fit a linear model for explainable inference. Moreover, we introduce residual calibration to address prediction errors stemming from linear models' insufficient expressiveness of complex LLM embeddings, thus recovering the LLM's predictive power and boosting overall accuracy. Theoretically, we provide a mathematical foundation to justify *MoleX*'s explainability. Extensive experiments demonstrate that *MoleX* outperforms existing methods in molecular property prediction, establishing a new milestone in predictive performance, explainability, and efficiency. In particular, *MoleX* enables CPU inference and accelerates large-scale dataset processing, achieving comparable performance 300$\times$ faster with 100,000 fewer parameters than LLMs. Additionally, the calibration improves model performance by up to 12.7% without compromising explainability. The source code is available at `https://github.com/MoleX2024/MoleX`.

1 INTRODUCTION

Molecular property prediction, aiming to analyze the relationship between molecular structures and properties, is crucial in various scientific domains, such as computational chemistry and biology (Xia et al., 2024; Yang et al., 2019). Deep learning advancements have significantly improved this field, showcasing the success of AI-driven problem-solving in science. Representative deep models for predicting molecular properties include graph neural networks (GNNs) (Lin et al., 2022; Wu et al., 2023b) and LLMs (Chithrananda et al., 2020; Ahmad et al., 2022). In particular, recently developed LLMs have exhibited remarkable performance by learning chemical semantics from text-based molecular representations, e.g., Simplified Molecular Input Line Entry Systems (SMILES) (Weininger, 1988). By capturing the chemical semantics and long-range dependencies in text-based molecules, LLMs show promising capabilities in providing accurate molecular property predictions (Ahmad et al., 2022). Nevertheless, the black-box nature of LLMs hinders the understanding of their decision-making mechanisms. Inevitably, this opacity prevents people from deriving reliable predictions and insights from these models (Wu et al., 2023a).

To narrow this gap, numerous explainable GNN and LLM methods have been proposed to identify molecular substructures that contribute to specific properties (Xiang et al., 2023; Proietti et al., 2024; Wang et al., 2024). Among these, Lamole (Wang et al., 2024) represents the state-of-the-art

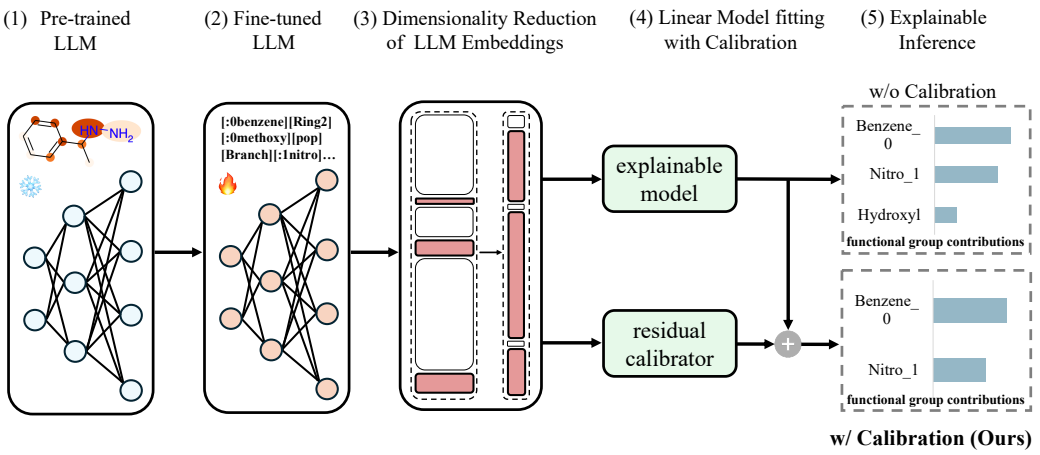

Figure 1: The framework of *MoleX* is divided into the following stages: (1) given ChemBERTa-2 as the pre-trained LLM, (2) fine-tune it on Group SELFIES (functional group-based molecular representation) with an information bottleneck-inspired objective to produce embeddings with maximum task-relevant information, (3) extract high-dimensional LLM embeddings and apply sparsity-inducing dimensionality reduction to exclude redundant information, (4) train a linear model using the preserved task-relevant information, (5) integrate the linear model with a residual calibrator that corrects prediction errors for explainable inference (see an algorithmic explanation in algorithm 1).

LLM-based approach attempting to provide both accurate predictions and chemically meaningful explanations—*chemical concepts-aligned substructures along with their interactions*. However, it still suffers from several flaws: *first*, the attention weights used for explanations do not correlate directly with feature importance (Jain and Wallace, 2019); *second*, it is model-specific due to varying implementations and interpretations of attention mechanisms across models (Voita et al., 2019); and *third*, the provided explanations are local, struggling to approximate global model decisions using established chemical concepts (Liu et al., 2022). Therefore, it is imperative to design a globally explainable method that delivers accurate predictions and identifies contributing substructures with their interactions for molecular property predictions.

This work proposes a new framework (illustrated in Figure 1), dubbed *MoleX*, that leverages a linear model augmented with LLM knowledge for explaining *complex, non-linear* molecular structure-property relationships, motivated by its simplicity and global explainability. To capture these complex relationships, *MoleX* extracts informative knowledge/embeddings from the LLM, which serve as inputs to fit a linear model. Moreover, we design information bottleneck-inspired fine-tuning and sparsity-inducing dimensionality reduction to maximize task-relevant information in LLM embeddings. Following prior work (Wang et al., 2024), we use Group SELFIES (Cheng et al., 2023)—a text-based molecular representation that partitions molecules into functional groups—as the LLM's input (as shown in appendix A.15). Group SELFIES enables LLMs to tokenize molecules into units of functional groups, aligning with chemical concepts at the substructure level. To quantify functional groups' contributions, we extract n-grams from Group SELFIES and feed them into the LLM, generating embeddings with semantically distinct functional groups for nuanced analysis. Notably, *MoleX*'s simplicity enables global explanations by approximating model behavior across the entire input space, rather than focusing on individual samples.

Although augmented with LLM knowledge, linear models still underfit complex non-linear relationships. To address this, we propose a residual calibration strategy that learns and corrects the linear model's residuals, iteratively bridging the gap between high-dimensional LLM embeddings and linear model's limited expressiveness by calibrating predictions. By iteratively driving residuals toward target values, the residual calibrator calibrates errors and restores the original LLM's predictive power. The linear model, augmented by LLM knowledge and a residual calibrator, achieves excellent predictive performance while retaining the explainability of linear models. In molecular context, the residual calibrator enables *MoleX* to iteratively correct mispredicted functional groups

and interactions, aligning predictions with domain expertise and leveraging chemically accurate substructures as explanations. Our contributions are summarized as

1. We propose *MoleX*, which extracts LLM knowledge to build a simple yet powerful linear model that identifies chemically meaningful substructures with their interactions for explainable molecular property predictions.
2. We develop optimization-based methods to maximize and preserve task-relevant information in LLM embeddings and theoretically demonstrate their explainability and validity.
3. We design a residual calibration strategy to correct linear model's prediction errors, improving both predictive and explanation performance.
4. We introduce n-gram coefficients, with a theoretical justification, to assess individual functional group contributions to molecular property predictions.

Experiments across 7 datasets demonstrate that *MoleX* achieves state-of-the-art classification and explanation accuracy while being 300× faster with 100,000 fewer parameters than alternative baselines, highlighting its superiority in predictive performance, explainability, and efficiency.

2 Related Work

Explainable Molecular Property Prediction. Given that molecules can be naturally represented as graphs, a collection of explainable GNNs have been proposed to explain the relationship between molecular structures and properties (Lin et al., 2021; Pope et al., 2019). However, these atom or bond-level explanations are not chemically meaningful to interpret their sophisticated relationships. Besides, through learning chemical semantics, the transformer-based LLMs can effectively capture interactions among substructures (Wang et al., 2024) and thus demonstrated their potential in understanding text-based molecules (Ross et al., 2022; Chithrananda et al., 2020). However, the opaque decision-making process of LLMs obscures their operating principles, risking unfaithful predictions with severe consequences, especially in high-stakes domains like drug discovery (Chen et al., 2024).

Explainability Methods for LLMs. To obtain trustworthy output, various techniques were introduced to unveil the LLM's explainability. The gradient-based explanations analyze the feature importance by computing output partial derivatives with respect to input (Sundararajan et al., 2017). These methods, nevertheless, lack robustness in their explanations due to sensitivity to data perturbations (Kindermans et al., 2019; Adebayo et al., 2018). The attention-based explanations use attention weights to interpret outputs (Hoover et al., 2020). Yet, recent studies challenge their reliability as attention weights may not consistently reflect true feature importance (Jain and Wallace, 2019; Serrano and Smith, 2019). The perturbation-based explanations elucidate model behaviors by observing output changes in response to input alterations (Ribeiro et al., 2016). However, these explanations are unstable due to the randomness of the perturbations (Agarwal et al., 2021). To resolve these issues, we extract informative embeddings from the LLM to fit a linear model for inference. This approach leverages both the LLM's knowledge and the linear model's explainability, offering reliable substructure-level explanations.

3 Preliminaries

Let $\mathcal{G} = \{(g^{(i)}, y^{(i)})\}$ be the dataset consisting of molecular graphs $g^{(i)}$ and their corresponding properties $y^{(i)}$. Our goal is to train a model f to map a molecular representation g to its property y, denoted as $f : g \mapsto y$. We first convert each molecular graph $g^{(i)}$ into Group SELFIES, denoted as $x^{(i)} = \{x_1^{(i)}, \ldots, x_{n^{(i)}}^{(i)}\}$, where $x_j^{(i)}$ is the j-th functional group, and $n^{(i)}$ is the number of functional groups in molecule i. For simplicity, we omit the superscript $^{(i)}$ in the following descriptions.

MoleX consists of two modules: an explainable model h and a residual calibrator r. After h predicts, its residuals are fed into r, which boosts performance without incurring any explainability impairment. We denote $f_H(x)$ and $f_R(x)$ as the features used by h and r, respectively, and $\mathcal{L}(\hat{y}, y)$ as the training loss. To learn h and r, we freeze the parameters of h and sequentially calibrate the mispredicted samples with the objective:

$$\min_{r} \ \mathbb{E}_{(x,y)\sim\mathcal{D}}\left[\mathcal{L}\left(h\left(f_H(x)\right)+r\left(f_R(x)\right),\, y\right)\right], \tag{3.1}$$

where $\mathcal{D}$ is the training dataset. Adapting the approach by Sebastiani (2002), we use n-gram coefficients in the linear model to measure the contributions of decoupled n-gram features (functional groups) to molecular properties. Let the n-gram feature x_j takes the coefficient w_j in the linear model; then its contribution score is computed as $c_j = w_j \cdot \text{Embedding}(x_j)$. This allows us to quantify the contribution of the j-th functional group to the property y. Our proof of the validity of using n-gram coefficients as contribution scores is provided in appendix A.2.

4 Our Framework: *MoleX*

MoleX does two things, i.e., (1) maximizing and preserving the task-relevant information in LLM embeddings via fine-tuning and dimensionality reduction and (2) extracting these embeddings to build a linear model with residual calibration. We thus divide it into two stages: LLM knowledge extraction and LLM-augmented linear model fitting. This section details our framework and provides theoretical foundations for its explainability.

4.1 LLM Knowledge Extraction with Improved Informativeness

Fine-tuning. To enhance the pre-trained LLM's understanding of functional group-based molecules, we fine-tune it on Group SELFIES data. However, extracting maximally informative embeddings from the LLM to augment the linear model's expressiveness is still challenging. We overcome this by incorporating the Variational Information Bottleneck (VIB) (Alemi et al., 2022) into the fine-tuning process, crafting a training loss that encourages the LLM to produce embeddings with maximum task-relevant information, thereby fully exploiting its internal knowledge. Particularly, given Group SELFIES inputs x, properties y, and LLM embeddings t, we define $p_0(t)$ as the prior distribution over t, and $q_\theta(y \mid t)$ as the variational approximation to the conditional distribution of the properties given the embeddings t. The mutual information between t and y is defined as:

$$I(t;y) = \mathbb{E}_{p(t,y)}\left[\log \frac{p(t,y)}{p(t)p(y)}\right] = \mathbb{E}_{p(t,y)}\left[\log \frac{p(y \mid t)}{p(y)}\right],$$

and the mutual information between t and x is defined as:

$$I(t;x) = \mathbb{E}_{p(t,x)}\left[\log \frac{p(t \mid x)}{p(t)}\right] = \mathbb{E}_{p(x)}\left[D_{\mathrm{KL}}\left(p_\theta(t \mid x) \,\middle\|\, p(t)\right)\right].$$

Since the marginal distribution $p(t)$ is intractable, we approximate it with the prior $p_0(t)$. Under this approximation, we use $D_{\mathrm{KL}}\left(p_\theta(t \mid x) \,\middle\|\, p_0(t)\right)$ as a tractable surrogate for $I(t;x)$, allowing us to minimize the mutual information between t and x. Inspired by Kingma et al. (2015), we approximate encoder $p_\theta(t \mid x)$ by a Gaussian distribution. Let $f_e^\mu(x)$ and $f_e^\Sigma(x)$ be neural networks that output the mean and covariance matrix of latent variable t. Then, the encoder is given as:

$$p_\theta(t \mid x) = \mathcal{N}\left(t \,\middle|\, f_e^\mu(x), f_e^\Sigma(x)\right).$$

Applying the reparameterization trick, we sample t as:

$$t = f_e^\mu(x) + f_e^\Sigma(x)^{1/2} \cdot \epsilon, \quad \text{where } \epsilon \sim \mathcal{N}(0, I).$$

Putting all these together, we design our training loss as:

$$\mathcal{L}(\theta) = \sum_{(x_i,y_i)\in\mathcal{S}_F} \left(\mathbb{E}_{p_\theta(t|x_i)}\left[-\log q_\theta(y_i \mid t)\right] + \beta \cdot D_{\mathrm{KL}}\left(p_\theta(t \mid x_i) \,\middle\|\, p_0(t)\right)\right), \tag{4.1}$$

where β is the tuning parameter between compression and performance, q_θ is the decoder (predictive model), and $\mathcal{S}_F$ is the dataset used for fine-tuning. In particular, the first component, $\mathbb{E}_{p_\theta(t|x_i)}[-\log q_\theta(y_i \mid t)]$, encourages the embeddings t to be informative about y by maximizing their predictive power. The second component, $\beta \cdot D_{\mathrm{KL}}(p_\theta(t \mid x_i) \parallel p_0(t))$, regularizes the embeddings to minimize redundant information from x, effectively promoting compression. Empirically, we use ChemBERTa-2 (Ahmad et al., 2022) as the foundation LLM for fine-tuning.

In essence, this objective ensures the fine-tuned LLM generates embeddings t that capture property-relevant information from y while compressing redundancy in x. Grounded in the information bottleneck principle, it produces informative embeddings (see our proof in appendix A.3.)

Theorem 4.1. *Let $\mathcal{L}(\theta)$ be the loss defined in eq.* (4.1)*. Under the assumptions of the reparameterization trick and the use of stochastic gradient descent, the optimization process converges to a local minimum that yields an informative representation t while retaining only the most relevant information from the task.*

Embedding Extraction. To capture individual functional group contributions and contextual information, we extract n-grams from Group SELFIES, with n selected via cross-validation. To ensure explainability, each n-gram is processed separately by the fine-tuned LLM using a functional group-level tokenizer, encoding a fixed-size embedding vector. These vectors are then aggregated into a single fixed-size embedding that encompasses semantics of all individual n-grams. More precisely, this single embedding contains all chemical semantics at the functional group level and represents the knowledge LLM learned during its training and fine-tuning.

4.2 Dimensionality-reduced embeddings for linear model fitting

Dimensionality Reduction. As the aggregated n-gram embeddings are high-dimensional and noisy, *eliminating the redundancy in them* becomes our new problem. Drawing inspiration from Lin et al. (2016), we design an explainable functional principal component analysis (EFPCA) that leads to effective dimensionality reduction. Accordingly, this preserves a compact yet informative feature set for the linear model. We formulate this dimensionality reduction as an optimization problem with a sparsity-inducing penalty, defined as:

Definition 4.1 (EFPCA)**.** *Let $X(t)$ be a stochastic process defined on a compact interval $[a, b]$ with mean function $\mu(t) = \mathbb{E}[X(t)]$. Assume that $X(t)$ has a covariance operator $\hat{\mathcal{C}}$ derived from the centered process $X(t) - \mu(t)$. The EFPCA seeks functions $\xi_k(t)$ that maximize the variance explained by the projections of $X(t)$ while promoting sparsity for explainability. Specifically, for each principal component indexed by k, the EFPCA solves:*

$$\max_{\xi_k} \left\{ \langle \xi_k, \hat{\mathcal{C}}\, \xi_k \rangle - \rho_k\, \mathcal{S}(\xi_k) \right\}$$

subject to $\|\xi_k\|_\gamma^2 = \|\xi_k\|^2 + \gamma \|\mathcal{D}^2 \xi_k\|^2 = 1$ and $\langle \xi_k, \xi_j \rangle_\gamma = 0$ for all $j < k$.

Here, $\|\xi_k\|^2 = \int_a^b \xi_k(t)^2\, dt$ is the squared L^2 norm, $\mathcal{D}^2$ denotes the second derivative operator, so $\mathcal{D}^2 \xi_k(t) = \dfrac{d^2 \xi_k(t)}{dt^2}$. The standard L^2 inner product is $\langle f, g \rangle = \int_a^b f(t) g(t)\, dt$, and the roughness-penalized inner product is $\langle f, g \rangle_\gamma = \langle f, g \rangle + \gamma \langle \mathcal{D}^2 f, \mathcal{D}^2 g \rangle$, where $\gamma > 0$ balances fit and smoothness. The parameter $\rho_k > 0$ controls sparsity. The function $\mathcal{S}(\xi_k) = \int_a^b \mathbf{1}_{\{\xi_k(t) \neq 0\}}\, dt$ measures the support length of $\xi_k(t)$. The index k specifies the principal components, with $k = 1, 2, \ldots$.

Since $\xi_k(t)$ is a linear combination of basis functions, we expand it using basis functions $\{\phi_j(t)\}_{j=1}^p$ with local support on sub-intervals $S_j \subset [a, b]$ as $\xi_k(t) = \sum_{j=1}^p a_{kj} \phi_j(t)$, where $a_k = (a_{k1}, \ldots, a_{kp})^\top$ are coefficients to be determined. In this finite-dimensional setting, the support length $\mathcal{S}(\xi_k)$ approximates to $\mathcal{S}(\xi_k) \approx \sum_{j=1}^p \mathbf{1}_{\{a_{kj} \neq 0\}} |S_j|$, which is proportional to the ℓ_0 "norm" of a_k, $\|a_k\|_0 = \sum_{j=1}^p \mathbf{1}_{\{a_{kj} \neq 0\}}$, assuming equal $|S_j|$. The ℓ_0 penalty $\rho_k \|a_k\|_0$ thus promotes sparsity by encouraging many coefficients a_{kj} to be zero when ρ_k is large, forcing $\xi_k(t)$ to be zero over extensive portions of $[a, b]$. Zero coefficients mean zero contributions from corresponding basis functions, so the optimization balances maximizing variance while minimizing the number of

nonzero coefficients, preserving significant components. As $\phi_j(t)$ have local support, nonzero a_{kj} correspond to specific intervals S_j, resulting in $\xi_k(t)$ being nonzero only over certain intervals. Thus, EFPCA produces sparse, explainable principal components due to their localized structure, highlighting regions where the data exhibits significant variation.

In summary, EFPCA offers a framework for explainable principal components, enabling effective dimensionality reduction. By combining a sparsity-inducing penalty with the local support of basis functions, the resulting principal components are sparse and capable of capturing informative features. Therefore, *MoleX* excludes irrelevant functional groups and identifies principal ones from high-dimensional embeddings. We thus formulate the theorem as (see our proof in appendix A.4):

Theorem 4.2. *The EFPCA produces sparse FPCs $\xi_k(t)$ that are exactly zero in intervals where the sample curves exhibit minimal variation. Consequently, the FPCs $\xi_k(t)$ are statistically explanatory, facilitating effective dimensionality reduction.*

Linear Model Fitting. Applying dimensionality-reduced n-gram embeddings as features, we train a logistic regression model for our classification tasks, which takes the form:

$$h(f_H(\mathbf{x})) = \sigma\left(\mathbf{w}^\top f_H(\mathbf{x}) + b\right) = \frac{1}{1 + e^{-(\mathbf{w}^\top f_H(\mathbf{x}) + b)}}, \tag{4.2}$$

where σ is the sigmoid function, $\mathbf{w} \in \mathbb{R}^n$ is the weight vector, $b \in \mathbb{R}$ is the bias term, and $f_H(\mathbf{x})$ is the explainable feature representation defined in eq. (3.1). In our setting, logistic regression is explainable since the log-odds transformation establishes a linear relationship between the features and the target variable, shown as $\log\left(\frac{h(f_H(\mathbf{x}))}{1-h(f_H(\mathbf{x}))}\right) = \mathbf{w}^\top f_H(\mathbf{x}) + b$. Differentiating with respect to a feature component $[f_H(\mathbf{x})]_j$ shows that each coefficient w_j quantifies the impact of that feature on the log-odds, shown as $\frac{\partial}{\partial [f_H(\mathbf{x})]_j} \log\left(\frac{h(f_H(\mathbf{x}))}{1-h(f_H(\mathbf{x}))}\right) = w_j$. Moreover, if f_H is a linear transformation, i.e., $f_H(\mathbf{x}) = \mathbf{C}\mathbf{x}$, the chain rule relates changes in the original features to the log-odds, which can be expressed as $\frac{\partial}{\partial x_j} \log\left(\frac{h(f_H(\mathbf{x}))}{1-h(f_H(\mathbf{x}))}\right) = \sum_{k=1}^{n} w_k C_{kj}$. Therefore, this linearity allows straightforward interpretation of each feature's influence on the predicted probabilities, making logistic regression highly explainable (Hastie et al., 2009).

Residual Calibration. The final step of *MoleX* involves training a residual calibrator r. With the parameters of the explainable model h frozen, the calibrator corrects mispredicted samples from h. By optimizing the objective in eq. (3.1), prediction errors are iteratively fixed, progressively aligning overall predictions with target values. Besides, to maintain explainability, the residual calibrator is designed as a linear model. Specifically, we define the residual calibrator r with weights $w_r \in \mathbb{R}^{d_r}$ corresponding to each residual feature and bias b_r:

$$r(f_R(x)) = w_r^\top f_R(x) + b_r.$$

Here, $f_R(x)$ represents the residual features obtained from the decomposition of the feature space $\mathbb{R}^d$ into orthogonal subspaces such that $f(x) = f_H(x) + f_R(x)$ with $f_H(x), f_R(x) \in \mathbb{R}^d$. The vector $f_H(x)$ contains the explainable features used by h and has non-zero components only in the index set $I_H \subseteq \{1, 2, \ldots, d\}$, while $f_R(x)$ contains the residual features used by r and has non-zero components only in the index set $I_R \subseteq \{1, 2, \ldots, d\}$, with $I_H \cap I_R = \emptyset$ and $I_H \cup I_R = \{1, 2, \ldots, d\}$. The orthogonality condition is given by $\langle f_H(x), f_R(x) \rangle = 0$, which holds because the supports of $f_H(x)$ and $f_R(x)$ are disjoint. Then, the overall prediction from h and r is given by:

$$\hat{y}(x) = \underbrace{w_h^\top f_H(x) + b_h}_{\text{Explainable Model Contribution}} + \underbrace{w_r^\top f_R(x) + b_r}_{\text{Residual Calibrator Contribution}},$$

where $w_h, w_r \in \mathbb{R}^d$ are the weight vectors for h and r, respectively, with w_h and w_r having non-zero components only in I_H and I_R, respectively. The orthogonality and linearity between $f_H(x)$ and $f_R(x)$ guarantee that the contributions from h and r are additive and independent, making the r explainable. Moreover, each feature's impact on the prediction can be directly understood through the corresponding weights in w_h and w_r. Since $f_H(x)$ and $f_R(x)$ are orthogonal, the inner products $w_h^\top f_R(x) = 0$ and $w_r^\top f_H(x) = 0$ vanish. This ensures that h and r do not influence each other's feature contributions, thus preserving the explainability of both models in the combined prediction. Empirically, both h and r update their parameters during prediction error calibration to enhance overall model performance. We formalize the following theorem (see our proof in appendix A.5):

Theorem 4.3. *Let $\mathcal{X}$ and $\mathcal{Y}$ be the input and output spaces, respectively. Let $f : \mathcal{X} \to \mathbb{R}^d$ be a pre-trained feature mapping, and let $h : \mathbb{R}^{d_c} \to \mathcal{Y}$ be an explainable linear model operating on the explainable features $f_H(x)$. The residual calibrator $r : \mathbb{R}^{d_r} \to \mathcal{Y}$, defined on the residual features $f_R(x)$, captures the variance not explained by h in an explainable manner, thereby preserving the overall model's explainability.*

Quantifiable Functional Group Contributions. As described in section 3, we measure the functional group x_j's contributions to molecular property y using n-gram coefficients. The molecular property y distributes its entire semantic information into individual functional groups x_j. Due to the linearity and additivity between x_j and y, the scalar coefficient w_j corresponding to x_j in the linear model weighs x_j's contributions to y in terms of chemical semantics. By taking the dot product of w_j and the embedding of x_j, we obtain a projection length of the functional group in the direction of weight vector, thus quantifying the impact of that functional group on the molecular property. Quantitatively, the larger the absolute value of an n-gram coefficient, the greater the contribution of the corresponding functional group to property. This metric provides a rigorous interpretation of feature contributions, ensuring unbiasedness and significance through OLS estimation (see our proof in appendix A.2). Using this method, we identify important functional groups from the LLM's complex embedding space. Furthermore, by incorporating n-gram coefficients and identified functional groups into the molecular graph, we can determine whether identified functional groups bond with each other and infer interactions among them. Based on this, *MoleX* reveals chemically meaningful substructures along with their interactions to faithfully explain molecular property predictions.

5 Experiments

5.1 Experimental Settings

Datasets. We empirically evaluate *MoleX*'s performance on six mutagenicity datasets and one hepatotoxicity dataset. The mutagenicity datasets include Mutag (Debnath et al., 1991), Mutagen (Morris et al., 2020), PTC family (i.e., PTC-FM, PTC-FR, PTC-MM, and PTC-MR) (Toivonen et al., 2003) and the hepatotoxicity dataset includes Liver (Liu et al., 2015). To demonstrate that *MoleX* can explain molecular properties using chemically meaningful substructures, we introduce the concept of ground truth: substructures verified by domain experts to have significant impacts on molecular properties. The ground truth substructures for six mutagenicity datasets are provided by Lin et al. (2022); Debnath et al. (1991), while those for the hepatotoxicity dataset are provided by Cheng et al. (2023). Further details are available in appendix A.6.

Evaluation Metrics. In this study, we evaluate the predictive performance, explainability performance, and computational efficiency of *MoleX*. Particularly, we apply a specific metric to assess each aspect of the model performance. For predictive performance, we define $\frac{1}{\mathrm{I}} \sum_{i=1}^{I} \mathbb{I}(y^{(i)} = \hat{y}^{(i)})$ to compute the classification accuracy. For explainability performance, we follow GNNExplainer (Ying et al., 2019), treating explanations as binary edge classification and using AUC to measure their accuracy. Noteworthily, as LLMs' probabilistic distributions over large vocabularies are incompatible with AUC's binary classification framework, we thus can not offer explanation accuracy for LLMs. For computational efficiency, we evaluate the execution time for each method.

Baselines. To extensively compare *MoleX* with different methods, we utilize (1) GNN baselines, including GCN (Kipf and Welling, 2016), DGCNN (Zhang et al., 2018), edGNN (Jaume et al., 2019), GIN (Xu et al., 2018), RW-GNN (Nikolentzos and Vazirgiannis, 2020), DropGNN (Papp et al., 2021), and IEGN (Maron et al., 2018); (2) LLM baselines, including Llama 3.1-8b (Dubey et al., 2024), GPT-4o (Achiam et al., 2023), and ChemBERTa-2 (Ahmad et al., 2022); (3) explainable model baselines, including logistic regression, decision tree (Quinlan, 1986), XGBoost (Chen and Guestrin, 2016), and random forest (Breiman, 2001).

Implementations. Our model is pre-trained on the full ZINC dataset (Irwin et al., 2012) using ChemBERTa-2, with 15% of tokens in each input randomly masked. We then fine-tune this model on the Mutag, Mutagen, PTC-FM, PTC-FR, PTC-MM, PTC-MR, and Liver datasets (in Group SELFIES). To evaluate model performance, we compute the average and standard deviation of each metric for each method after 20 rounds of execution. Further details are provided in appendix A.7.

Table 1: Classification accuracy over seven datasets (%). The best results are highlighted in **bold**.

Methods	Mutag	Mutagen	PTC-FM	PTC-FR	PTC-MM	PTC-MR	Liver
GCN (Kipf and Welling, 2016)	83.4± 0.4	77.2± 0.7	56.5± 0.3	62.7± 0.5	58.3± 0.2	52.1± 0.6	40.6± 0.3
DGCNN (Zhang et al., 2018)	86.2± 0.2	73.7± 0.5	56.1± 0.4	64.0± 0.8	61.8± 0.7	57.1± 0.6	45.4± 0.9
edGNN (Jaume et al., 2019)	85.4± 0.6	76.5± 0.3	58.7± 0.4	66.3± 0.7	65.2± 0.6	55.1± 0.8	43.7± 0.4
GIN (Xu et al., 2018)	86.1± 0.3	81.0± 0.5	63.4± 0.8	67.8± 0.6	66.5± 0.4	65.5± 0.4	45.2± 0.9
RW-GNN (Nikolentzos and Vazirgiannis, 2020)	88.2± 0.6	79.6± 0.2	60.5± 0.7	63.2± 0.5	61.1± 0.4	58.2± 0.6	42.9± 0.3
DropGNN (Papp et al., 2021)	90.3± 0.5	82.2± 0.3	61.4± 0.8	65.3± 0.6	62.9± 0.2	63.5± 0.7	46.1± 0.6
IEGN (Maron et al., 2018)	83.9± 0.4	79.3± 0.5	61.9± 0.4	60.1± 0.3	62.1± 0.4	60.7± 0.5	44.8± 0.8
LLAMA3.1-8b (Dubey et al., 2024)	67.6± 3.4	50.7± 3.6	49.6± 2.6	46.2± 3.8	42.0± 2.8	47.5± 2.8	42.2± 2.2
GPT-4o (Achiam et al., 2023)	73.5± 3.6	51.2± 0.5	52.7± 2.3	53.8± 2.9	48.8± 2.4	53.7± 1.8	44.5± 2.5
ChemBERTa-2 (Ahmad et al., 2022)	87.3± 2.7	77.6± 2.2	59.2± 1.9	64.8± 2.2	59.7± 2.8	59.8± 2.4	46.3± 2.3
Logistic Regression	58.3± 1.2	55.4± 0.8	48.4± 1.1	48.3± 1.0	48.7± 1.1	44.9± 1.0	32.5± 0.5
Decision Tree (Quinlan, 1986)	60.8± 1.7	58.6± 1.5	43.3± 1.0	46.1± 0.7	47.2± 0.7	43.5± 0.5	36.9± 0.8
Random Forest (Breiman, 2001)	64.6± 1.9	60.6± 1.5	46.9± 1.2	51.4± 1.5	51.3± 1.8	46.4± 1.1	34.8± 1.9
XGBoost (Chen and Guestrin, 2016)	66.9± 1.2	67.6± 1.4	51.4± 1.3	53.1± 1.4	55.8± 1.2	49.3± 2.1	38.5± 1.8
w/o Calibration	86.1± 2.2	74.4± 1.0	59.7± 2.1	68.9± 1.9	69.3± 2.7	61.2± 2.4	45.0± 2.0
w/ Calibration (Ours)	**91.6± 2.0**	**83.7± 0.9**	**64.2± 1.4**	**74.4± 1.9**	**76.4± 1.8**	**68.4± 2.3**	**54.9± 2.4**

Table 2: Explanation accuracy over seven datasets (%). The best results are highlighted in **bold**.

Methods	Mutag	Mutagen	PTC-FM	PTC-FR	PTC-MM	PTC-MR	Liver
GCN (Kipf and Welling, 2016)	81.1± 0.2	76.4± 0.2	65.3± 0.4	67.8± 0.7	70.8± 0.8	65.1± 0.2	62.8± 0.2
DGCNN (Zhang et al., 2018)	86.3± 1.2	87.1± 0.5	63.0± 1.3	57.0± 1.2	63.0± 1.3	62.3± 0.8	67.5± 1.6
edGNN (Jaume et al., 2019)	**94.7± 0.9**	74.4± 0.7	65.9± 0.5	64.1± 0.5	66.6± 0.7	61.4± 0.7	63.2± 0.3
GIN (Xu et al., 2018)	92.1± 0.2	75.6± 0.3	67.5± 0.6	69.2± 0.5	68.5± 0.8	61.3± 0.5	68.3± 0.9
RW-GNN (Nikolentzos and Vazirgiannis, 2020)	89.9± 0.6	76.7± 0.2	65.8± 0.3	55.5± 0.3	66.9± 0.1	59.3± 0.2	64.7± 0.5
DropGNN (Papp et al., 2021)	83.4± 0.2	77.4± 0.3	68.4± 0.2	64.7± 0.4	63.2± 0.2	57.4± 0.7	64.5± 0.8
IEGN (Maron et al., 2018)	82.0± 0.2	77.5± 0.2	61.6± 0.6	62.6± 0.9	69.3± 0.7	59.1± 0.7	66.6± 0.6
Logistic Regression	59.2± 0.4	50.6± 0.9	54.4± 0.3	47.7± 0.8	49.9± 0.7	44.3± 0.7	53.8± 0.7
Decision Tree (Quinlan, 1986)	61.2± 0.2	55.7± 1.0	56.7± 0.8	46.4± 1.1	48.1± 0.9	39.9± 0.8	56.4± 1.0
Random Forest (Breiman, 2001)	66.7± 1.2	57.2± 1.2	59.9± 1.7	50.9± 1.2	55.0± 0.8	46.6± 1.1	60.7± 1.4
XGBoost (Chen and Guestrin, 2016)	65.2± 1.2	61.3± 1.1	58.5± 1.8	49.4± 1.8	51.6± 1.3	50.2± 0.8	69.0± 1.4
w/o Calibration	90.0± 0.9	77.7± 1.0	68.0± 1.7	66.6± 1.1	62.0± 1.5	67.5± 1.5	72.0± 2.0
w/ Calibration (Ours)	92.6± 1.7	**89.0± 1.2**	**77.9± 1.5**	**79.3± 1.4**	**72.3± 1.7**	**73.4± 1.3**	**80.3± 1.4**

5.2 RESULTS

Predictive Performance. Table 1 presents a comparison of predictive performance across different methods. *MoleX* outperforms all baselines, showing robustness and generalizability. By combining LLMs with explainable models, it achieves 16.9% and 23.1% higher average accuracy than LLM and explainable model baselines, proving the effectiveness of augmenting explainable models with LLM knowledge. Moreover, by integrating residual calibration, *MoleX* raises the average classification accuracy by 7.0% across seven datasets. Notably, the classification accuracy of our base model, logistic regression, improves by 27.8% after LLM knowledge augmentation and then by an additional 5.5% after residual calibration on the Mutag dataset. Therefore, by maximizing task-relevant semantic information in the LLM knowledge and employing a residual calibration strategy, we enable a simple linear model to achieve predictive performance even superior to that of GNNs and LLMs in molecular property predictions.

Explainability Performance. Table 2 summarizes the explanation accuracy of different methods. Be encoding functional group-based molecules, *MoleX* achieves significantly better explainability than baselines. Residual calibration further enhances explainability, improving average accuracy by 8.8%. It achieves this by iteratively correcting mispredicted functional groups and leveraging chemically accurate ones with their interactions to explain molecular properties. On the Mutag, the explanation accuracy of logistic regression is boosted by 33.4% via LLM knowledge augmentation and residual calibration. Interestingly, while others excel on simpler datasets like Mutag but falter on complex ones, *MoleX* achieves 13.2% higher classification and 16.9% higher explanation accuracy on Liver. It highlights *MoleX*'s capability of representing the complexity of molecular data.

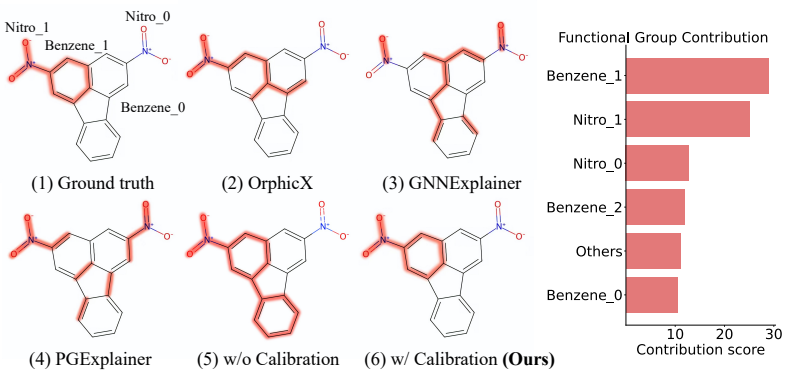

Figure 2: Explanation visualization of a molecule from the Mutag dataset (left), and the contribution scores of the identified functional groups offered by *MoleX* (right).

Figure 2 visualizes the explanation for a randomly selected molecule from the Mutag dataset. The ground truth, verified by domain experts, shows that mutagenicity arises from an aromatic functional group (e.g., benzene ring) bonded with another group like nitro or carbonyl. *MoleX* precisely identifies this ground truth substructure, faithfully explaining molecular structure-property relationships. In contrast, other methods only identify a collection of individual atoms and bonds, failing to recognize chemically meaningful substructures as a whole. For instance, PGExplainer identifies single atoms from multiple benzene rings, whereas atoms alone are insufficient to explain overall molecular properties. Notably, *MoleX* **without** calibration identifies two additional elements beyond the ground truth, thus suggesting the significance of residual calibration to explanation accuracy. Moreover, contribution scores elucidate interactions among functional groups, with the benzene-nitro substructure on the upper left receiving a high score, showcasing its importance to mutagenicity as a bonded/interacting entity. More explanation visualizations are in appendix A.12.

Computational Efficiency. Figure 3 displays the inference time of different methods. Unlike methods that rely on iterative optimization in neural networks, *MoleX* enables considerably faster inference. Generally, *MoleX* outperforms both GNNs (at least $15\times$ faster) and LLMs (at least $120\times$ faster) in speed while achieving higher classification and explanation accuracy. *MoleX* consistently costs the least inference times across all datasets, reinforcing its scalability for real-world applications and large-scale computations on molecular data. In addition to faster inference, *MoleX* also significantly reduces GPU memory usage compared to baselines by avoiding numerous iterative parameter updates and storage in optimization algorithms. Consequently, the inference power of the linear model is critically augmented by LLM knowledge and residual calibration while preserving the advantage of explainability and computational efficiency.

5.3 Ablation Studies

In this section, we introduce ablation studies on the number of n in n-gram, principal components in EFPCA, training iterations of the residual calibrator, and the selection of the base model.

Number of n in N-grams. We empirically compare the choice of n in n-grams. As shown in fig. 6, the overall model performance improves as n increases from 1 to 3, then declines for n from 4 to 9. Three of four datasets in our studies indicate the optimal performance at $n = 3$. Increasing n captures more contextual semantics, including functional group interactions and raises the model performance. However, overlarge n values incorporate excessive or irrelevant contextual information and reduce model utility correspondingly. Further details are in appendix A.11.

Dimensionality Reduction via EFPCA. We use EFPCA to reduce the dimensionality of LLM embeddings, obtaining explainable and compact embeddings. As shown in fig. 5, cross-validation across four datasets determines the optimal number of principal components. Empirically, components beyond 20 contribute minimally to the molecular property prediction. Additional components yield diminishing returns while increasing model complexity and reducing explainability. Further details are in appendix A.9. Moreover, we also investigate the effect of our dimensionality reduction. As presented in table 5, we compare the model performance **without** dimensionality reduction. We

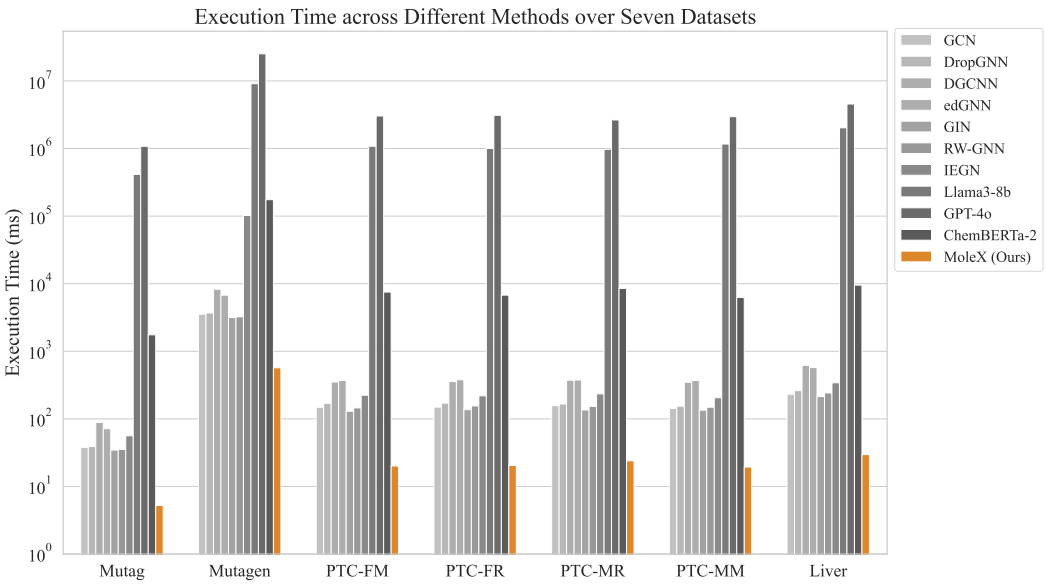

Figure 3: Execution time across different methods over seven datasets. Ours achieves the best inference efficiency.

find that models using only 20 principal components achieve performance within 5% of models using all components. This means selected components effectively preserve task-relevant information while excluding redundancy. Further details are offered in appendix A.10.

Training Iterations of the Residual Calibrator. We apply the training objective in 3.1 to learn a residual calibrator that iteratively fix prediction errors. As shown in fig. 4, we observe that the model performance improves substantially with increasing training iterations until reaching a threshold. Beyond this point, the model overfits the data, leading to a performance decline. This finding suggests the need for an appropriate stopping criterion to balance model performance and prevent overfitting. Empirically, the optimal number of training iterations is 5. Further details and a theoretical demonstration are offered in appendix A.8.

Selection of the Base Model. Aside from the logistic regression, we examine the effect of LLM augmentation using other statistical learning models as the base model. The classification and explanation accuracy are reported in table 6 and table 7, respectively. All statistical learning models augmented with LLM knowledge and residual calibration outperform GNNs and LLMs. Besides, more complicated models, like XGBoost and random forest, achieve better performance in both classification and explanation accuracy than simple models like LASSO. Therefore, LLM knowledge is capable of augmenting a model on top of its original predictive capabilities, evidencing the effectiveness and generalizability of our method. However, model complexity generally trades off with explainability. Considering this, we select the logistic regression as our base model for its optimal balance between explainability and performance. Further details are offered in appendix A.13.

6 Conclusion

This work presents *MoleX*, a framework leveraging LLM knowledge to train a linear model for accurate molecular property predictions with chemically meaningful explanations. Using information bottleneck-inspired fine-tuning and sparsity-based dimensionality reduction, *MoleX* extracts task-relevant knowledge for explainable inference. Furthermore, a residual calibration module further boosts performance by correcting prediction errors. During its inference, *MoleX* precisely reveals crucial substructures with their interactions as explanations. Notably, *MoleX* enjoys the advantage of LLM's predictive power while preserving the linear model's intrinsic explainability. Extensive theoretical and empirical justification demonstrate *MoleX*'s exceptional predictive performance, explainability, and efficiency.

REFERENCES

Josh Achiam, Steven Adler, Sandhini Agarwal, Lama Ahmad, Ilge Akkaya, Florencia Leoni Aleman, Diogo Almeida, Janko Altenschmidt, Sam Altman, Shyamal Anadkat, et al. Gpt-4 technical report. *arXiv preprint arXiv:2303.08774*, 2023.

Julius Adebayo, Justin Gilmer, Michael Muelly, Ian Goodfellow, Moritz Hardt, and Been Kim. Sanity checks for saliency maps. *Advances in neural information processing systems*, 31, 2018.

Sushant Agarwal, Shahin Jabbari, Chirag Agarwal, Sohini Upadhyay, Steven Wu, and Himabindu Lakkaraju. Towards the unification and robustness of perturbation and gradient based explanations. In *International Conference on Machine Learning*, pages 110–119. PMLR, 2021.

Walid Ahmad, Elana Simon, Seyone Chithrananda, Gabriel Grand, and Bharath Ramsundar. Chemberta-2: Towards chemical foundation models. *arXiv preprint arXiv:2209.01712*, 2022.

Alexander A Alemi, Ian Fischer, Joshua V Dillon, and Kevin Murphy. Deep variational information bottleneck. In *International Conference on Learning Representations*, 2022.

Leo Breiman. Random forests. *Machine learning*, 45:5–32, 2001.

Jialin Chen, Shirley Wu, Abhijit Gupta, and Rex Ying. D4explainer: In-distribution explanations of graph neural network via discrete denoising diffusion. *Advances in Neural Information Processing Systems*, 36, 2024.

Tianqi Chen and Carlos Guestrin. Xgboost: A scalable tree boosting system. In *Proceedings of the 22nd acm sigkdd international conference on knowledge discovery and data mining*, pages 785–794, 2016.

Austin H Cheng, Andy Cai, Santiago Miret, Gustavo Malkomes, Mariano Phielipp, and Alán Aspuru-Guzik. Group selfies: a robust fragment-based molecular string representation. *Digital Discovery*, 2(3):748–758, 2023.

Seyone Chithrananda, Gabriel Grand, and Bharath Ramsundar. Chemberta: Large-scale self-supervised pretraining for molecular property prediction. *arXiv preprint arXiv:2010.09885*, 2020.

Asim Kumar Debnath, Rosa L Lopez de Compadre, Gargi Debnath, Alan J Shusterman, and Corwin Hansch. Structure-activity relationship of mutagenic aromatic and heteroaromatic nitro compounds. correlation with molecular orbital energies and hydrophobicity. *Journal of medicinal chemistry*, 34(2):786–797, 1991.

Abhimanyu Dubey, Abhinav Jauhri, Abhinav Pandey, Abhishek Kadian, Ahmad Al-Dahle, Aiesha Letman, Akhil Mathur, Alan Schelten, Amy Yang, Angela Fan, et al. The llama 3 herd of models. *arXiv preprint arXiv:2407.21783*, 2024.

Trevor Hastie, Robert Tibshirani, Jerome H Friedman, and Jerome H Friedman. *The elements of statistical learning: data mining, inference, and prediction*, volume 2. Springer, 2009.

Benjamin Hoover, Hendrik Strobelt, and Sebastian Gehrmann. exbert: A visual analysis tool to explore learned representations in transformer models. In *Proceedings of the 58th Annual Meeting of the Association for Computational Linguistics: System Demonstrations*, pages 187–196, 2020.

John J Irwin, Teague Sterling, Michael M Mysinger, Erin S Bolstad, and Ryan G Coleman. Zinc: a free tool to discover chemistry for biology. *Journal of chemical information and modeling*, 52 (7):1757–1768, 2012.

Sarthak Jain and Byron C Wallace. Attention is not explanation. In *Proceedings of the 2019 Conference of the North American Chapter of the Association for Computational Linguistics: Human Language Technologies, Volume 1 (Long and Short Papers)*, pages 3543–3556, 2019.

Guillaume Jaume, An-Phi Nguyen, Maria Rodriguez Martinez, Jean-Philippe Thiran, and Maria Gabrani. edgnn: A simple and powerful gnn for directed labeled graphs. In *International Conference on Learning Representations*, 2019.

Pieter-Jan Kindermans, Sara Hooker, Julius Adebayo, Maximilian Alber, Kristof T Schütt, Sven Dähne, Dumitru Erhan, and Been Kim. The (un) reliability of saliency methods. *Explainable AI: Interpreting, explaining and visualizing deep learning*, pages 267–280, 2019.

Durk P Kingma, Tim Salimans, and Max Welling. Variational dropout and the local reparameterization trick. *Advances in neural information processing systems*, 28, 2015.

Thomas N Kipf and Max Welling. Semi-supervised classification with graph convolutional networks. In *International Conference on Learning Representations*, 2016.

Wanyu Lin, Hao Lan, and Baochun Li. Generative causal explanations for graph neural networks. In *International Conference on Machine Learning*, pages 6666–6679. PMLR, 2021.

Wanyu Lin, Hao Lan, Hao Wang, and Baochun Li. Orphicx: A causality-inspired latent variable model for interpreting graph neural networks. In *Proceedings of the IEEE/CVF Conference on Computer Vision and Pattern Recognition*, pages 13729–13738, 2022.

Zhenhua Lin, Liangliang Wang, and Jiguo Cao. Interpretable functional principal component analysis. *Biometrics*, 72(3):846–854, 2016.

Ruifeng Liu, Xueping Yu, and Anders Wallqvist. Data-driven identification of structural alerts for mitigating the risk of drug-induced human liver injuries. *Journal of cheminformatics*, 7:1–8, 2015.

Yibing Liu, Haoliang Li, Yangyang Guo, Chenqi Kong, Jing Li, and Shiqi Wang. Rethinking attention-model explainability through faithfulness violation test. In *International Conference on Machine Learning*, pages 13807–13824. PMLR, 2022.

Dongsheng Luo, Wei Cheng, Dongkuan Xu, Wenchao Yu, Bo Zong, Haifeng Chen, and Xiang Zhang. Parameterized explainer for graph neural network. *Advances in neural information processing systems*, 33:19620–19631, 2020.

Haggai Maron, Heli Ben-Hamu, Nadav Shamir, and Yaron Lipman. Invariant and equivariant graph networks. In *International Conference on Learning Representations*, 2018.

Nourollah Mirghaffari, Riccardo Iannarelli, Christian Ludwig, and Michel J Rossi. Coexistence of reactive functional groups at the interface of a powdered activated amorphous carbon: a molecular view. *Molecular Physics*, 119(17-18):e1966110, 2021.

Christopher Morris, Nils M Kriege, Franka Bause, Kristian Kersting, Petra Mutzel, and Marion Neumann. Tudataset: A collection of benchmark datasets for learning with graphs. *arXiv preprint arXiv:2007.08663*, 2020.

Giannis Nikolentzos and Michalis Vazirgiannis. Random walk graph neural networks. *Advances in Neural Information Processing Systems*, 33:16211–16222, 2020.

Pál András Papp, Karolis Martinkus, Lukas Faber, and Roger Wattenhofer. Dropgnn: Random dropouts increase the expressiveness of graph neural networks. *Advances in Neural Information Processing Systems*, 34:21997–22009, 2021.

Phillip E Pope, Soheil Kolouri, Mohammad Rostami, Charles E Martin, and Heiko Hoffmann. Explainability methods for graph convolutional neural networks. In *Proceedings of the IEEE/CVF conference on computer vision and pattern recognition*, pages 10772–10781, 2019.

Michela Proietti, Alessio Ragno, Biagio La Rosa, Rino Ragno, and Roberto Capobianco. Explainable ai in drug discovery: self-interpretable graph neural network for molecular property prediction using concept whitening. *Machine Learning*, 113(4):2013–2044, 2024.

J. Ross Quinlan. Induction of decision trees. *Machine learning*, 1:81–106, 1986.

Marco Tulio Ribeiro, Sameer Singh, and Carlos Guestrin. " why should i trust you?" explaining the predictions of any classifier. In *Proceedings of the 22nd ACM SIGKDD international conference on knowledge discovery and data mining*, pages 1135–1144, 2016.

Jerret Ross, Brian Belgodere, Vijil Chenthamarakshan, Inkit Padhi, Youssef Mroueh, and Payel Das. Large-scale chemical language representations capture molecular structure and properties. *Nature Machine Intelligence*, 4(12):1256–1264, 2022.

Fabrizio Sebastiani. Machine learning in automated text categorization. *ACM computing surveys (CSUR)*, 34(1):1–47, 2002.

Sofia Serrano and Noah A Smith. Is attention interpretable? In *Proceedings of the 57th Annual Meeting of the Association for Computational Linguistics*, pages 2931–2951, 2019.

Mukund Sundararajan, Ankur Taly, and Qiqi Yan. Axiomatic attribution for deep networks. In *International conference on machine learning*, pages 3319–3328. PMLR, 2017.

Hannu Toivonen, Ashwin Srinivasan, Ross D King, Stefan Kramer, and Christoph Helma. Statistical evaluation of the predictive toxicology challenge 2000–2001. *Bioinformatics*, 19(10):1183–1193, 2003.

Elena Voita, David Talbot, Fedor Moiseev, Rico Sennrich, and Ivan Titov. Analyzing multi-head self-attention: Specialized heads do the heavy lifting, the rest can be pruned. In *Proceedings of the 57th Annual Meeting of the Association for Computational Linguistics*, pages 5797–5808, 2019.

Zhenzhong Wang, Zehui Lin, Wanyu Lin, Ming Yang, Minggang Zeng, and Kay Chen Tan. Explainable Molecular Property Prediction: Aligning Chemical Concepts with Predictions via Language Models. *arXiv preprint arXiv:2405.16041*, 2024.

David Weininger. Smiles, a chemical language and information system. 1. introduction to methodology and encoding rules. *Journal of chemical information and computer sciences*, 28(1):31–36, 1988.

Zhenxing Wu, Jihong Chen, Yitong Li, Yafeng Deng, Haitao Zhao, Chang-Yu Hsieh, and Tingjun Hou. From black boxes to actionable insights: a perspective on explainable artificial intelligence for scientific discovery. *Journal of Chemical Information and Modeling*, 63(24):7617–7627, 2023a.

Zhenxing Wu, Jike Wang, Hongyan Du, Dejun Jiang, Yu Kang, Dan Li, Peichen Pan, Yafeng Deng, Dongsheng Cao, Chang-Yu Hsieh, et al. Chemistry-intuitive explanation of graph neural networks for molecular property prediction with substructure masking. *Nature Communications*, 14(1): 2585, 2023b.

Jun Xia, Lecheng Zhang, Xiao Zhu, Yue Liu, Zhangyang Gao, Bozhen Hu, Cheng Tan, Jiangbin Zheng, Siyuan Li, and Stan Z Li. Understanding the limitations of deep models for molecular property prediction: Insights and solutions. *Advances in Neural Information Processing Systems*, 36, 2024.

Yan Xiang, Yu-Hang Tang, Guang Lin, and Daniel Reker. Interpretable molecular property predictions using marginalized graph kernels. *Journal of Chemical Information and Modeling*, 63(15): 4633–4640, 2023.

Keyulu Xu, Weihua Hu, Jure Leskovec, and Stefanie Jegelka. How powerful are graph neural networks? In *International Conference on Learning Representations*, 2018.

Kevin Yang, Kyle Swanson, Wengong Jin, Connor Coley, Philipp Eiden, Hua Gao, Angel Guzman-Perez, Timothy Hopper, Brian Kelley, Miriam Mathea, et al. Analyzing learned molecular representations for property prediction. *Journal of chemical information and modeling*, 59(8):3370–3388, 2019.

Zhitao Ying, Dylan Bourgeois, Jiaxuan You, Marinka Zitnik, and Jure Leskovec. Gnnexplainer: Generating explanations for graph neural networks. *Advances in neural information processing systems*, 32, 2019.

Muhan Zhang, Zhicheng Cui, Marion Neumann, and Yixin Chen. An end-to-end deep learning architecture for graph classification. In *Proceedings of the AAAI conference on artificial intelligence*, volume 32, 2018.

A APPENDIX

A.1 ALGORITHMIC EXPLANATIONS FOR *MoleX*'S WORKFLOW

We offer the pseudo code describing the training and inference of *MoleX* as shown in algorithm 1.

Algorithm 1 Training and Inference Procedure for *MoleX*

Input: Dataset $\mathcal{S}_D = \{(x_i, y_i)\}$ where x_i are input Group SELFIES, y_i are molecular properties.

Split dataset: $\mathcal{S}_D = \mathcal{S}_{\text{train}} \cup \mathcal{S}_{\text{eval}} \cup \mathcal{S}_{\text{test}}$

for each x_i in $\mathcal{S}_D$ **do**

Extract n-gram features:

$$x_i^{\text{ngram}} = \text{N-Gram}(x_i)$$

Obtain embeddings from fine-tuned LLM:

$$x_i^{\text{emb}} = \text{Extract}\left(x_i^{\text{ngram}}\right)$$

Dimensionality reduction via EFPCA:

$$\tilde{x}_i = \text{EFPCA}\left(x_i^{\text{emb}}\right)$$

Train explainable model h:

Train h by minimizing:

$$h = \arg\min_h \sum_{i \in \mathcal{S}_{\text{train}}} \mathcal{L}\left(h\left(f_H\left(\tilde{x}_i\right)\right),\ y_i\right)$$

Compute residuals on $\mathcal{S}_{\text{eval}}$:

for each $i \in \mathcal{S}_{\text{eval}}$ **do**

Compute residual:

$$y_{r,i} = y_i - h\left(f_H\left(\tilde{x}_i\right)\right)$$

Train residual calibrator r:

Train r by minimizing:

$$r = \arg\min_r \sum_{i \in \mathcal{S}_{\text{eval}}} \mathcal{L}\left(r\left(f_R\left(\tilde{x}_i\right)\right),\ y_{r,i}\right)$$

Make final predictions on $\mathcal{S}_{\text{test}}$:

for each $i \in \mathcal{S}_{\text{test}}$ **do**

Compute final prediction:

$$\hat{y}_i = \text{Aggregate}\left(h\left(f_H\left(\tilde{x}_i\right)\right),\ r\left(f_R\left(\tilde{x}_i\right)\right)\right)$$

A.2 PROOF OF N-GRAM COEFFICIENTS AS VALID CONTRIBUTION SCORES FOR DECOUPLED N-GRAM FEATURES

In this section, we demonstrate that n-gram coefficients in the linear model can be interpreted as feature contribution scores based on the statistical properties of the linear model.

Proof. Suppose $\mathbf{E} \in \mathbb{R}^{n \times d}$ is the matrix of n-gram embeddings, where each row $\mathbf{e}_i^\top$ is the embedding of the i-th n-gram. Let $\mathbf{v}_{ij} \in \mathbb{R}^d$ be the embedding of the j-th feature in the i-th n-gram, and suppose that each n-gram consists of m features (we assume m is a constant across all n-grams for simplicity). Let c_{ij} denote the contribution score of the j-th feature in the i-th n-gram.

We formulate the following linearity assumptions to ensure the validity of using n-gram coefficients as contribution scores:

- **Linearity.** The relationship between the input embeddings and the output is linear. Namely, for all i,
$$y_i = \mathbf{e}_i^\top \mathbf{w}^* + \epsilon_i,$$
where $\mathbf{w}^* \in \mathbb{R}^d$ is the true coefficient vector, and ϵ_i is the error term.
- **N-gram Embedding Decomposition.** Each n-gram embedding $\mathbf{e}_i$ is the average of its constituent feature embeddings:
$$\mathbf{e}_i = \frac{1}{m} \sum_{j=1}^{m} \mathbf{v}_{ij}.$$
- **Ordinary Least Squares (OLS).** The linear model is estimated using OLS by minimizing the residual sum of squares:
$$\hat{\mathbf{w}} = \arg\min_{\mathbf{w}} \sum_{i=1}^{n} (y_i - \mathbf{e}_i^\top \mathbf{w})^2.$$
- **Error Properties.**
  (a) **Zero Mean Errors.** The errors ϵ_i have zero mean given the embeddings:
  $$\mathbb{E}[\epsilon_i \mid \mathbf{E}] = 0.$$
  (b) **Homoscedasticity.** The errors have constant variance given the embeddings:
  $$\mathrm{Var}[\epsilon_i \mid \mathbf{E}] = \sigma^2,$$
  where $\sigma^2 > 0$ is a constant.
  (c) **No Autocorrelation.** The errors are uncorrelated with each other:
  $$\mathrm{Cov}[\epsilon_i, \epsilon_j \mid \mathbf{E}] = 0 \quad \text{for } i \neq j.$$
- **Full Rank.** The matrix $\mathbf{E}^\top \mathbf{E}$ is invertible (i.e., $\mathbf{E}$ has full column rank).

We define the contribution score of each decoupled n-gram feature as follows:

Definition A.1. *The* feature contribution score c_{ij} *for the* j*-th feature in the* i*-th n-gram is defined as*
$$c_{ij} = \mathbf{v}_{ij}^\top \hat{\mathbf{w}},$$
where $\hat{\mathbf{w}}$ *is the estimated coefficient vector from the linear model.*

Lemma A.1 (Prediction as Sum of Feature Contributions)**.** *Under Assumption A.2, the predicted output for the* i*-th n-gram is*
$$\hat{y}_i = \mathbf{e}_i^\top \hat{\mathbf{w}} = \frac{1}{m} \sum_{j=1}^{m} c_{ij}.$$

Proof. Using the embedding decomposition and the definition of the contribution scores, we have
$$\begin{aligned}
\hat{y}_i &= \mathbf{e}_i^\top \hat{\mathbf{w}} \\
&= \left(\frac{1}{m} \sum_{j=1}^{m} \mathbf{v}_{ij} \right)^\top \hat{\mathbf{w}} \\
&= \frac{1}{m} \sum_{j=1}^{m} \mathbf{v}_{ij}^\top \hat{\mathbf{w}} \\
&= \frac{1}{m} \sum_{j=1}^{m} c_{ij}.
\end{aligned}$$
This completes the proof. □

Theorem A.2 (Contribution Scores Quantify Individual Feature Contributions)**.** *Under the Linearity assumption (Assumption A.2), the feature contribution scores c_{ij} quantify the contributions of individual features to the prediction $\hat{y}_i$.*

Proof. From Lemma A.1, the predicted value $\hat{y}_i$ is given as the average of the feature contribution scores c_{ij}:

$$\hat{y}_i = \frac{1}{m} \sum_{j=1}^{m} c_{ij}.$$

This equation shows that each feature's contribution score c_{ij} directly influences the prediction $\hat{y}_i$. Therefore, c_{ij} quantifies the contribution of the j-th feature in the i-th n-gram to the prediction.

This completes the proof. □

Due to the statistical properties of the OLS estimator, we formulate the following theorem:

Theorem A.3 (Properties of the OLS Estimator)**.** *Under Assumptions A.2–A.2, the OLS estimator $\hat{\mathbf{w}}$ satisfies:*

1. ***Unbiasedness.*** $\mathbb{E}[\hat{\mathbf{w}} \mid \mathbf{E}] = \mathbf{w}^*$.
2. ***Variance-Covariance Matrix.*** $\mathrm{Var}[\hat{\mathbf{w}} \mid \mathbf{E}] = \sigma^2(\mathbf{E}^\top \mathbf{E})^{-1}$.
3. ***Consistency.*** *As $n \to \infty$,* $\hat{\mathbf{w}} \xrightarrow{P} \mathbf{w}^*$.

Proof. We prove each property as follows.

(1) Unbiasedness: The OLS estimator is given by

$$\hat{\mathbf{w}} = (\mathbf{E}^\top \mathbf{E})^{-1} \mathbf{E}^\top \mathbf{y}.$$

Substituting $\mathbf{y} = \mathbf{E}\mathbf{w}^* + \boldsymbol{\epsilon}$, we have

$$\hat{\mathbf{w}} = \mathbf{w}^* + (\mathbf{E}^\top \mathbf{E})^{-1} \mathbf{E}^\top \boldsymbol{\epsilon}.$$

Taking expectations conditional on $\mathbf{E}$ and using Assumption A.2(a),

$$\mathbb{E}[\hat{\mathbf{w}} \mid \mathbf{E}] = \mathbf{w}^* + (\mathbf{E}^\top \mathbf{E})^{-1} \mathbf{E}^\top \mathbb{E}[\boldsymbol{\epsilon} \mid \mathbf{E}] = \mathbf{w}^*.$$

(2) Variance-Covariance Matrix: The variance conditional on $\mathbf{E}$ is

$$\begin{aligned} \mathrm{Var}[\hat{\mathbf{w}} \mid \mathbf{E}] &= \mathrm{Var}\left((\mathbf{E}^\top \mathbf{E})^{-1} \mathbf{E}^\top \boldsymbol{\epsilon} \mid \mathbf{E}\right) \\ &= (\mathbf{E}^\top \mathbf{E})^{-1} \mathbf{E}^\top \mathrm{Var}[\boldsymbol{\epsilon} \mid \mathbf{E}] \mathbf{E} (\mathbf{E}^\top \mathbf{E})^{-1} \\ &= \sigma^2 (\mathbf{E}^\top \mathbf{E})^{-1}, \end{aligned}$$

using Assumptions A.2(b) and (c).

(3) Consistency: As $n \to \infty$, under the Law of Large Numbers,

$$\frac{1}{n} \mathbf{E}^\top \mathbf{E} \xrightarrow{P} \mathbf{Q},$$

where $\mathbf{Q}$ is positive definite due to Assumption A.2. Additionally,

$$\frac{1}{n} \mathbf{E}^\top \boldsymbol{\epsilon} \xrightarrow{P} \mathbf{0},$$

since $\boldsymbol{\epsilon}$ has zero mean and finite variance. Therefore,

$$\hat{\mathbf{w}} = \mathbf{w}^* + (\mathbf{E}^\top \mathbf{E})^{-1} \mathbf{E}^\top \boldsymbol{\epsilon} \xrightarrow{P} \mathbf{w}^*.$$

This completes the proof. □

To validate the convergence of the contribution scores, we introduce the asymptotic normality of the OLS estimator.

Corollary A.1 (Asymptotic Normality)**.** *If the error terms $\boldsymbol{\epsilon}$ are independently and identically normally distributed with mean zero and variance σ^2, then we have*

$$\sqrt{n}(\hat{\mathbf{w}} - \mathbf{w}^*) \xrightarrow{d} \mathcal{N}\left(\mathbf{0}, \sigma^2 \mathbf{Q}^{-1}\right),$$

where $\mathbf{Q} = \lim_{n\to\infty} \frac{1}{n}\mathbf{E}^\top \mathbf{E}$.

Proof. Under the given conditions, the Central Limit Theorem applies to $\mathbf{E}^\top \boldsymbol{\epsilon}$. Specifically,

$$\sqrt{n}(\hat{\mathbf{w}} - \mathbf{w}^*) = (\mathbf{E}^\top \mathbf{E})^{-1}\mathbf{E}^\top \boldsymbol{\epsilon} = \left(\frac{1}{n}\mathbf{E}^\top \mathbf{E}\right)^{-1} \left(\frac{1}{\sqrt{n}}\mathbf{E}^\top \boldsymbol{\epsilon}\right).$$

As $n \to \infty$, $\frac{1}{n}\mathbf{E}^\top \mathbf{E} \xrightarrow{P} \mathbf{Q}$ and $\frac{1}{\sqrt{n}}\mathbf{E}^\top \boldsymbol{\epsilon} \xrightarrow{d} \mathcal{N}(\mathbf{0}, \sigma^2 \mathbf{Q})$. Therefore,

$$\sqrt{n}(\hat{\mathbf{w}} - \mathbf{w}^*) \xrightarrow{d} \mathcal{N}\left(\mathbf{0}, \sigma^2 \mathbf{Q}^{-1}\right).$$

This completes the proof. □

Lemma A.4 (Variance of $\hat{c}_{ij}$)**.** *The variance of the estimated feature contribution score $\hat{c}_{ij} = \mathbf{v}_{ij}^\top \hat{\mathbf{w}}$ is*

$$\mathrm{Var}[\hat{c}_{ij} \mid \mathbf{E}] = \sigma^2 \mathbf{v}_{ij}^\top (\mathbf{E}^\top \mathbf{E})^{-1} \mathbf{v}_{ij}.$$

Proof. Since $\hat{c}_{ij}$ is a linear function of $\hat{\mathbf{w}}$, its variance conditional on $\mathbf{E}$ is

$$\begin{aligned}
\mathrm{Var}[\hat{c}_{ij} \mid \mathbf{E}] &= \mathrm{Var}\left(\mathbf{v}_{ij}^\top \hat{\mathbf{w}} \mid \mathbf{E}\right) \\
&= \mathbf{v}_{ij}^\top \mathrm{Var}[\hat{\mathbf{w}} \mid \mathbf{E}] \mathbf{v}_{ij} \\
&= \sigma^2 \mathbf{v}_{ij}^\top (\mathbf{E}^\top \mathbf{E})^{-1} \mathbf{v}_{ij},
\end{aligned}$$

using the result from Theorem A.3(2).

This completes the proof. □

Finally, we demonstrate the statistical significance of the feature contribution scores based on the n-gram coefficients.

Theorem A.5 (t-Statistic for Feature Contribution Scores)**.** *Under the above assumptions, the t-statistic for testing $H_0 : c_{ij} = 0$ is given by*

$$t_{ij} = \frac{\hat{c}_{ij}}{\mathrm{SE}[\hat{c}_{ij}]} = \frac{\mathbf{v}_{ij}^\top \hat{\mathbf{w}}}{\sigma \sqrt{\mathbf{v}_{ij}^\top (\mathbf{E}^\top \mathbf{E})^{-1} \mathbf{v}_{ij}}}.$$

Proof. The standard error of $\hat{c}_{ij}$ is

$$\mathrm{SE}[\hat{c}_{ij}] = \sqrt{\mathrm{Var}[\hat{c}_{ij} \mid \mathbf{E}]} = \sigma \sqrt{\mathbf{v}_{ij}^\top (\mathbf{E}^\top \mathbf{E})^{-1} \mathbf{v}_{ij}}.$$

Therefore, the t-statistic is

$$t_{ij} = \frac{\hat{c}_{ij}}{\mathrm{SE}[\hat{c}_{ij}]}.$$

Under the null hypothesis $H_0 : c_{ij} = 0$ and assuming normality of the errors, t_{ij} follows a t-distribution with $n - d$ degrees of freedom.

This completes the proof. □

From Theorem A.2, we have shown that the feature contribution scores c_{ij} represent the contributions of individual features to the predictions $\hat{y}_i$. The statistical properties outlined in Theorem A.3 and Lemma A.4 guarantee that these estimates are reliable and that their statistical significance can be assessed.

Therefore, we conclude that each feature's contribution to the prediction can be quantified by its corresponding coefficient in the linear model, enabling us to assess the importance of individual features. By mathematically linking the model coefficients to the feature contributions, we validate the use of these coefficients as measures of feature importance. We also establish that using n-gram coefficients derived from feature embeddings and model coefficients as contribution scores for input features is valid and grounded in the statistical properties of the linear model.

By expressing the predicted output as the sum of individual feature contributions, we effectively decouple the influence of each feature or functional group on the output or molecular property. This decoupling allows us to isolate the effect of each n-gram feature or functional group x on the molecular property y. Consequently, the contribution scores c_{ij} provide a quantitative measure of how each functional group impacts the molecular property.

This completes the proof.

□

A.3 Proof of theorem 4.1 (Demonstration of VIB-based Training Objectives)

Proof. We demonstrate the Variational Information Bottleneck (VIB) framework, which aims to learn a compressed representation Z of the input variable X that preserves maximal information about the target variable Y while being minimally informative about X itself. This is achieved by optimizing the objective function as follows:

$$\mathcal{L}_{\text{IB}}(\theta) = I(Z;X) - \beta I(Z;Y)$$

where $I(\cdot;\cdot)$ is mutual information, $\beta \geq 0$ is a tuning parameter, and θ represents the parameters of the encoder. Our goal is to derive a tractable variational lower bound of this objective function that can be optimized using stochastic gradient descent.

Definition A.2 (Mutual Information)**.** *For random variables X and Z with joint distribution $p(X, Z)$, the mutual information $I(X;Z)$ is defined as*

$$I(X;Z) = \mathbb{E}_{p(X,Z)}\left[\log \frac{p(X,Z)}{p(X)p(Z)}\right]$$

Alternatively, it can be expressed as

$$I(X;Z) = \mathbb{E}_{p(X)}\left[D_{\text{KL}}(p(Z \mid X) \| p(Z))\right]$$

Definition A.3 (Kullback-Leibler Divergence)**.** *For probability distributions P and Q over the same probability space, the KL divergence from Q to P is defined as*

$$D_{\text{KL}}(P\|Q) = \int p(x) \log \frac{p(x)}{q(x)}\, dx = \mathbb{E}_{p(x)}\left[\log \frac{p(x)}{q(x)}\right]$$

Definition A.4 (Conditional Entropy)**.** *The conditional entropy $H(Y \mid Z)$ is defined as*

$$H(Y \mid Z) = -\mathbb{E}_{p(Z,Y)}\left[\log p(Y \mid Z)\right]$$

We then formulate the problem. Let $\mathcal{D} = \{(X_i, Y_i)\}_{i=1}^N$ be a dataset of input-output pairs sampled from an unknown distribution $p(X, Y)$. The encoder $p_\theta(Z \mid X)$ parameterizes the conditional

distribution of Z given X, and the decoder $q_\phi(Y \mid Z)$ parameterizes the conditional distribution of Y given Z. Our objective is to optimize the parameters θ and ϕ by maximizing the Information Bottleneck Lagrangian as follows:

$$\mathcal{L}_{\text{IB}}(\theta, \phi) = I(Z; Y) - \beta I(Z; X)$$

However, direct computation of $I(Z; Y)$ and $I(Z; X)$ is intractable. Therefore, we derive variational bounds to make the optimization objective tractable. We start by applying the following lemma:

Lemma A.6 (Variational Upper Bound on $I(Z; X)$)**.** *The mutual information $I(Z; X)$ can be upper-bounded as*

$$I(Z; X) \leq \mathbb{E}_{p(X)} \left[D_{\text{KL}}(p_\theta(Z \mid X) \| r(Z)) \right]$$

where $r(Z)$ is an arbitrary prior distribution over Z.

Proof. We start by expressing $I(Z; X)$ as

$$I(Z; X) = \mathbb{E}_{p(X)} \left[D_{\text{KL}}(p_\theta(Z \mid X) \| p(Z)) \right]$$

Since $p(Z) = \int p_\theta(Z \mid X) p(X) \, dX$ is intractable, we introduce an arbitrary prior $r(Z)$ and consider:

$$I(Z; X) = \mathbb{E}_{p(X)} \left[D_{\text{KL}}(p_\theta(Z \mid X) \| r(Z)) - D_{\text{KL}}(p(Z) \| r(Z)) \right]$$

Here, we utilize the identity:

$$D_{\text{KL}}(p_\theta(Z \mid X) \| p(Z)) = D_{\text{KL}}(p_\theta(Z \mid X) \| r(Z)) - D_{\text{KL}}(p(Z) \| r(Z))$$

since

$$\mathbb{E}_{p(X)} \left[D_{\text{KL}}(p_\theta(Z \mid X) \| p(Z)) \right] = \mathbb{E}_{p(X)} \left[D_{\text{KL}}(p_\theta(Z \mid X) \| r(Z)) \right] - D_{\text{KL}}(p(Z) \| r(Z))$$

Since $D_{\text{KL}}(p(Z) \| r(Z)) \geq 0$, it follows that:

$$I(Z; X) \leq \mathbb{E}_{p(X)} \left[D_{\text{KL}}(p_\theta(Z \mid X) \| r(Z)) \right]$$

This completes the proof. □

Lemma A.7 (Variational Lower Bound on $I(Z; Y)$)**.** *The mutual information $I(Z; Y)$ can be lower-bounded as*

$$I(Z; Y) \geq \mathbb{E}_{p(X,Y)} \left[\mathbb{E}_{p_\theta(Z|X)} \left[\log q_\phi(Y \mid Z) \right] \right] - H(Y)$$

Proof. By the definition of mutual information:

$$I(Z; Y) = H(Y) - H(Y \mid Z) = H(Y) + \mathbb{E}_{p(Z,Y)} \left[\log p(Y \mid Z) \right]$$

Since $p(Y \mid Z)$ is generally intractable, we introduce a variational approximation $q_\phi(Y \mid Z)$ and leverage Jensen's inequality:

$$\mathbb{E}_{p(Z,Y)} \left[\log p(Y \mid Z) \right] \geq \mathbb{E}_{p(Z,Y)} \left[\log q_\phi(Y \mid Z) \right]$$

Therefore:

$$I(Z;Y) \geq H(Y) + \mathbb{E}_{p(Z,Y)} \left[\log q_\phi(Y \mid Z)\right]$$

Rewriting the expectation over $p(Z,Y)$ as an expectation over $p(X,Y)$ and $p_\theta(Z \mid X)$, we have:

$$I(Z;Y) \geq H(Y) + \mathbb{E}_{p(X,Y)} \left[\mathbb{E}_{p_\theta(Z|X)} \left[\log q_\phi(Y \mid Z)\right]\right]$$

Thus:

$$I(Z;Y) \geq \mathbb{E}_{p(X,Y)} \left[\mathbb{E}_{p_\theta(Z|X)} \left[\log q_\phi(Y \mid Z)\right]\right] - H(Y)$$

This completes the proof. □

Now we can formulate the Variational Information Bottleneck (VIB) objective. By combining Lemmas A.6 and A.7, we obtain a tractable objective function.

Proposition A.8 (Variational Upper Bound on the Information Bottleneck Objective)**.** *The Information Bottleneck Lagrangian can be upper-bounded by the variational objective function:*

$$\mathcal{L}(\theta,\phi) = \mathbb{E}_{p(X,Y)} \left[\mathbb{E}_{p_\theta(Z|X)} \left[-\log q_\phi(Y \mid Z)\right] + \beta\, D_{\mathrm{KL}}(p_\theta(Z \mid X) \| r(Z))\right]$$

Proof. Starting from the original objective:

$$\mathcal{L}_{\mathrm{IB}}(\theta,\phi) = I(Z;X) - \beta I(Z;Y)$$

Applying the upper bound of $I(Z;X)$ from Lemma A.6 and the lower bound of $I(Z;Y)$ from Lemma A.7, we get:

$$\begin{aligned}\mathcal{L}_{\mathrm{IB}}(\theta,\phi) &\leq \mathbb{E}_{p(X)} \left[D_{\mathrm{KL}}(p_\theta(Z \mid X) \| r(Z))\right] - \beta \left(\mathbb{E}_{p(X,Y)} \left[\mathbb{E}_{p_\theta(Z|X)} \left[\log q_\phi(Y \mid Z)\right]\right] - H(Y)\right) \\ &= \mathbb{E}_{p(X)} \left[D_{\mathrm{KL}}(p_\theta(Z \mid X) \| r(Z))\right] + \beta H(Y) - \beta\, \mathbb{E}_{p(X,Y)} \left[\mathbb{E}_{p_\theta(Z|X)} \left[\log q_\phi(Y \mid Z)\right]\right]\end{aligned}$$

Since $H(Y)$ is constant with respect to θ and ϕ, we can ignore it for optimization purposes. Thus, we define the variational objective function as:

$$\mathcal{L}(\theta,\phi) = \mathbb{E}_{p(X,Y)} \left[\mathbb{E}_{p_\theta(Z|X)} \left[-\log q_\phi(Y \mid Z)\right] + \beta\, D_{\mathrm{KL}}(p_\theta(Z \mid X) \| r(Z))\right]$$

By minimizing $\mathcal{L}(\theta,\phi)$, we effectively minimize an upper bound on $\mathcal{L}_{\mathrm{IB}}(\theta,\phi)$, satisfying our optimization goal.

This completes the proof. □

In our fine-tuning stage, since the expectation over $p(X,Y)$ is approximated by empirical samples from the dataset $\mathcal{D}$, and the expectations over $p_\theta(Z \mid X)$ are approximated by Monte Carlo sampling using the reparameterization trick. Thus, the loss function is expressed as (this is a generalized form of our designed loss function shown in (4.1)):

$$\hat{\mathcal{L}}(\theta,\phi) = \frac{1}{N} \sum_{i=1}^{N} \left(-\mathbb{E}_{p_\theta(Z|X_i)} \left[\log q_\phi(Y_i \mid Z)\right] + \beta\, D_{\mathrm{KL}}(p_\theta(Z \mid X_i) \| r(Z))\right)$$

To demonstrate convergence, we formulate the following theorem:

Theorem A.9 (Convergence of Stochastic Gradient Descent)**.** *Under standard assumptions of stochastic optimization (e.g., bounded gradients, appropriate learning rates, smoothness conditions), stochastic gradient descent (SGD) converges to a local minimum of $\hat{\mathcal{L}}(\theta,\phi)$.*

Proof. While neural network training is non-convex, empirical and theoretical results in optimization suggest that SGD can converge to critical points (which may be local minima, maxima, or saddle points) provided the loss function is smooth (i.e., continuously differentiable) and the gradients are Lipschitz continuous. Given that $\hat{\mathcal{L}}(\theta, \phi)$ is composed of differentiable functions, and the gradients with respect to θ and ϕ can be computed via backpropagation, convergence to a local minimum is attainable under proper settings of the learning rate and optimization parameters.

This completes the proof. □

We express the following corollary regarding our learned molecular representation after fine-tuning:

Corollary A.2 (Informative and Compressed Molecular Representation)**.** *At convergence, the learned representation Z satisfies:*

$$I(Z;Y) \text{ is maximized, and } I(Z;X) \text{ is minimized (subject to the tuning parameter } \beta)$$

Proof. By optimizing the variational objective function $\hat{\mathcal{L}}(\theta, \phi)$, we are effectively minimizing an upper bound on $I(Z;X)$ (Lemma A.6) and maximizing a lower bound on $I(Z;Y)$ (Lemma A.7). The trade-off between the two objectives is controlled by β.

As β increases, more emphasis is placed on minimizing $I(Z;X)$, leading to a more compressed representation Z that preserves only the most task-relevant information about Y.

This completes the proof. □

Specifically, as the first term in the loss function encourages the embeddings t to be highly predictive of y, it intrinsically captures the task-relevant information. Meanwhile, the second term penalizes the complexity of t by forcing it to be close to the prior $p_0(t)$, thereby excluding unnecessary information from x. These objectives ensure that the embeddings are both task-relevant and compact, containing minimal spurious data. Additionally, through the derivation of variational bounds and the construction of a tractable objective function, we have shown that minimizing $\mathcal{L}(\theta, \phi)$ allows us to learn a molecular representation Z that captures maximal information about Y while being minimally informative about X, in accordance with the Information Bottleneck principle. The optimization of $\mathcal{L}$ via SGD converges to a local minimum under standard optimization assumptions. Therefore, we learn an informative embedding after fine-tuning the pre-trained LLM, and we thus can extract the embedding with improved informativeness.

In conclusion, by framing the fine-tuning within the VIB framework, we derive this approach that balances the essential information for property prediction y with the elimination of irrelevant details from the input molecular representation x. This theoretical foundation ensures that our method effectively focuses on extracting the most relevant features needed for accurate predictions.

This completes the proof. □

A.4 Proof of theorem 4.2 (Explainability of EFPCA)

Proof. To demonstrate the explainability of the EFPCA method, we will show how the incorporation of a sparsity-inducing penalty and the use of basis functions with local support lead to functional principal components (FPCs) that are both sparse and localized, enhancing interpretability.

First, we formulate the EFPCA as an optimization problem. The EFPCA seeks to find FPCs $\xi_k(t)$ that maximize the variance of the projections of the centered stochastic process $X(t) - \mu(t)$ onto $\xi_k(t)$, while promoting sparsity for explainability. Specifically, for each principal component indexed by k, we solve:

$$\max_{\xi_k} \left\{ \langle \xi_k, \hat{\mathcal{C}}\, \xi_k \rangle - \rho_k\, \mathcal{S}(\xi_k) \right\} \tag{A.1}$$

subject to the normalization constraint:

$$\|\xi_k\|_\gamma^2 = \|\xi_k\|^2 + \gamma \left\|\mathcal{D}^2 \xi_k\right\|^2 = 1, \tag{A.2}$$

and the orthogonality constraints:

$$\langle \xi_k, \xi_j \rangle_\gamma = 0 \quad \text{for all } j < k. \tag{A.3}$$

Here $\hat{\mathcal{C}}$ is the empirical covariance operator of the centered process $X(t) - \mu(t)$, defined by $\hat{\mathcal{C}} f = \int_a^b \hat{c}(t,s) f(s)\, ds$, where $\hat{c}(t,s)$ is the empirical covariance function. $\langle f, g \rangle = \int_a^b f(t)\, g(t)\, dt$ is the standard L^2 inner product. $\|f\|^2 = \langle f, f \rangle$ is the squared L^2 norm. $\mathcal{D}^2 f = \dfrac{d^2 f(t)}{dt^2}$ denotes the second derivative of $f(t)$. $\|\mathcal{D}^2 f\|^2 = \langle \mathcal{D}^2 f, \mathcal{D}^2 f \rangle$ penalizes the roughness of $f(t)$. $\gamma > 0$ is a smoothing parameter balancing variance explanation and smoothness. $\langle f, g \rangle_\gamma = \langle f, g \rangle + \gamma \langle \mathcal{D}^2 f, \mathcal{D}^2 g \rangle$ is the roughness-penalized inner product. $\mathcal{S}(\xi_k) = \int_a^b \mathbf{1}_{\{\xi_k(t) \neq 0\}}\, dt$ measures the length of the support of $\xi_k(t)$, promoting sparsity. $\rho_k > 0$ controls the sparsity of $\xi_k(t)$. k is the index of the principal component, with $k = 1, 2, \ldots$.

Then, we construct an expansion of $\xi_k(t)$ using basis functions with local support. Let $\{\phi_j(t)\}_{j=1}^p$ be a set of basis functions that have local support on the interval $[a, b]$, such as B-spline basis functions. Each $\phi_j(t)$ is nonzero only over a subinterval $S_j \subset [a, b]$. We express $\xi_k(t)$ as a linear combination of these basis functions:

$$\xi_k(t) = \sum_{j=1}^p a_{kj} \phi_j(t), \tag{A.4}$$

where $a_k = (a_{k1}, a_{k2}, \ldots, a_{kp})^\top$ is the coefficient vector for the k-th principal component. We substitute the expansion (A.4) into the optimization problem (A.1). To express the objective function and constraints in terms of a_k, we compute the variance explained by $\xi_k(t)$:

$$\langle \xi_k, \hat{\mathcal{C}}\, \xi_k \rangle = \left\langle \sum_{i=1}^p a_{ki} \phi_i, \hat{\mathcal{C}} \sum_{j=1}^p a_{kj} \phi_j \right\rangle = \sum_{i=1}^p \sum_{j=1}^p a_{ki} a_{kj} \langle \phi_i, \hat{\mathcal{C}} \phi_j \rangle.$$

We define the matrix $\mathbf{Q} \in \mathbb{R}^{p \times p}$ with entries $Q_{ij} = \langle \phi_i, \hat{\mathcal{C}} \phi_j \rangle$, so the variance term becomes $a_k^\top \mathbf{Q} a_k$. The sparsity-inducing term $\mathcal{S}(\xi_k)$ approximates to:

$$\mathcal{S}(\xi_k) \approx \sum_{j=1}^p \mathbf{1}_{\{a_{kj} \neq 0\}} |S_j|,$$

assuming negligible overlap between the supports of different $\phi_j(t)$, where $|S_j|$ is the length of the support of $\phi_j(t)$. If the supports are of equal length or normalized, we can consider $\mathcal{S}(\xi_k) \propto \|a_k\|_0$, where $\|a_k\|_0 = \sum_{j=1}^p \mathbf{1}_{\{a_{kj} \neq 0\}}$ counts the number of nonzero coefficients.

Therefore, the objective function becomes:

$$\text{Objective:} \quad a_k^\top \mathbf{Q} a_k - \rho_k \|a_k\|_0. \tag{A.5}$$

We have the roughness-penalized norm is:

$$\|\xi_k\|_\gamma^2 = \langle \xi_k, \xi_k \rangle + \gamma \langle \mathcal{D}^2 \xi_k, \mathcal{D}^2 \xi_k \rangle = a_k^\top \mathbf{G} a_k,$$

where $\mathbf{G} = \mathbf{G}_0 + \gamma \mathbf{G}_2$, with $\mathbf{G}_0$ having entries $(\mathbf{G}_0)_{ij} = \langle \phi_i, \phi_j \rangle$, and $\mathbf{G}_2$ having entries $(\mathbf{G}_2)_{ij} = \langle \mathcal{D}^2 \phi_i, \mathcal{D}^2 \phi_j \rangle$. Thus, the normalization constraint becomes:

$$a_k^\top \mathbf{G} a_k = 1. \tag{A.6}$$

Additionally, the orthogonality constraints with respect to the roughness-penalized inner product are given as:

$$\langle \xi_k, \xi_j \rangle_\gamma = a_k^\top \mathbf{G} a_j = 0, \quad \text{for all } j < k.$$

Combining these, the optimization problem becomes:

$$\max_{a_k} \left\{ a_k^\top \mathbf{Q} a_k - \rho_k \|a_k\|_0 \right\} \tag{A.7}$$

subject to:

$$a_k^\top \mathbf{G} a_k = 1, \quad \text{and} \quad a_k^\top \mathbf{G} a_j = 0 \quad \text{for all } j < k. \tag{A.8}$$

The term $\rho_k \|a_k\|_0$ in the objective function is an ℓ_0 penalty that promotes sparsity in the coefficient vector a_k. When ρ_k is large, the optimization favors solutions with fewer nonzero coefficients, effectively selecting only the most significant basis functions. We define the index set of nonzero coefficients:

$$\mathcal{I}_k = \{ j \mid a_{kj} \neq 0 \}. \tag{A.9}$$

The principal component $\xi_k(t)$ then simplifies to:

$$\xi_k(t) = \sum_{j \in \mathcal{I}_k} a_{kj} \phi_j(t). \tag{A.10}$$

Since each $\phi_j(t)$ has support only on S_j, the support of $\xi_k(t)$ is given by:

$$\text{supp}(\xi_k) = \bigcup_{j \in \mathcal{I}_k} S_j. \tag{A.11}$$

Thus, $\xi_k(t)$ is exactly zero outside these intervals, and nonzero only over regions where significant variation is captured by the selected basis functions. The localization of $\xi_k(t)$ enhances explainability in several ways:

- **Identification of Significant Intervals.** The nonzero coefficients a_{kj} correspond to basis functions whose supports S_j cover intervals where the data exhibits important features. This directly highlights regions of interest in the functional data.
- **Simplification of Interpretation.** By reducing the number of nonzero coefficients, $\xi_k(t)$ becomes simpler and easier to interpret, focusing on key patterns in the data.
- **Exclusion of Irrelevant Information.** The sparsity induced by the ℓ_0 penalty effectively filters out noise and redundant information, ensuring that only meaningful variations are considered.

Moreover, the roughness penalty $\gamma \|\mathcal{D}^2 \xi_k\|^2$ ensures that $\xi_k(t)$ remains smooth within its support, avoiding overfitting and maintaining the functional integrity of the principal components. The parameter γ balances the trade-off between fitting the data closely and keeping the principal components smooth.

In the context of high-dimensional embeddings from LLMs, the EFPCA method effectively reduces dimensionality while enhancing explainability. By promoting sparsity, it preserves only the most informative features associated with the task, filtering out task-irrelevant information present in the

embeddings. The localized structure of $\xi_k(t)$ allows for direct interpretation of the components in terms of specific intervals or features in the data.

In conclusion, the incorporation of a sparsity-inducing ℓ_0 penalty and the use of basis functions with local support in the EFPCA framework lead to principal components that are both sparse and localized. This results in FPCs $\xi_k(t)$ that are nonzero only over intervals where the data contains significant variation, making them intrinsically explainable. The optimization framework balances variance maximization, sparsity, and smoothness, yielding components that facilitate effective dimensionality reduction while providing clear insights into the underlying functional data. In our implementation, we maintain statistically significant features in an explainable manner, ensuring that the dimensionality reduction aids in both performance and interpretability.

This completes the proof. □

A.5 Proof of theorem A.10 (Explainability of Residual Calibration)

Proof. We demonstrate that the residual calibrator r is explainable when combined with the explainable linear model h, under the conditions of linearity and orthogonality.

Let $\mathcal{X}$ and $\mathcal{Y}$ be the input and output spaces, respectively. Let $f : \mathcal{X} \to \mathbb{R}^d$ be a pre-trained feature mapping that extracts features from the inputs $x \in \mathcal{X}$. We decompose the feature vector $f(x)$ into two components:

$$f(x) = f_H(x) + f_R(x),$$

where $f_H(x), f_R(x) \in \mathbb{R}^d$ are the explainable and residual features, respectively. The vector $f_H(x)$ contains the explainable features used by the explainable model h, and has non-zero components only in the index set $I_H \subseteq \{1, 2, \ldots, d\}$. Similarly, $f_R(x)$ contains the residual features used by the residual calibrator r, and has non-zero components only in the index set $I_R \subseteq \{1, 2, \ldots, d\}$, with $I_H \cap I_R = \emptyset$ and $I_H \cup I_R = \{1, 2, \ldots, d\}$. To ensure orthogonality between $f_H(x)$ and $f_R(x)$, we observe that their supports are disjoint, implying that their inner product is zero:

$$\langle f_H(x), f_R(x) \rangle = \sum_{i=1}^{d} [f_H(x)]_i \cdot [f_R(x)]_i = 0,$$

since for each i, at least one of $[f_H(x)]_i$ or $[f_R(x)]_i$ is zero. The explainable model $h : \mathbb{R}^d \to \mathcal{Y}$ is defined as a linear model operating on $f_H(x)$:

$$h(f_H(x)) = w_h^\top f_H(x) + b_h,$$

where $w_h \in \mathbb{R}^d$ is the weight vector with non-zero components only in I_H, and $b_h \in \mathbb{R}$ is the bias term. Similarly, the residual calibrator $r : \mathbb{R}^d \to \mathcal{Y}$ is defined as a linear model operating on $f_R(x)$:

$$r(f_R(x)) = w_r^\top f_R(x) + b_r,$$

where $w_r \in \mathbb{R}^d$ is the weight vector with non-zero components only in I_R, and $b_r \in \mathbb{R}$ is the bias term. The overall prediction from h and r is given by:

$$\hat{y}(x) = h(f_H(x)) + r(f_R(x)) = w_h^\top f_H(x) + b_h + w_r^\top f_R(x) + b_r.$$

We define the combined weight vector $w = w_h + w_r \in \mathbb{R}^d$ and combined bias $b = b_h + b_r$, so the prediction simplifies to:

$$\hat{y}(x) = w^\top f(x) + b.$$

Due to the orthogonality of $f_H(x)$ and $f_R(x)$, and the disjoint supports of w_h and w_r, the cross terms vanish:

$$w_h^\top f_R(x) = \sum_{i \in I_H} [w_h]_i [f_R(x)]_i = 0, \quad w_r^\top f_H(x) = \sum_{i \in I_R} [w_r]_i [f_H(x)]_i = 0,$$

since $[w_h]_i = 0$ for $i \notin I_H$ and $[f_R(x)]_i = 0$ for $i \in I_H$, and similarly for w_r and $f_H(x)$. This ensures that h and r do not influence each other's feature contributions, thus preserving the explainability of both models in the combined prediction. To illustrate how r captures the variance not explained by h in an explainable manner, consider that the residual calibrator r corrects mispredicted samples from h by fitting to the residuals $y - h(f_H(x))$. By optimizing the objective:

$$\min_r \mathbb{E}_{(x,y)\sim\mathcal{D}} \left[\mathcal{L} \left(h(f_H(x)) + r(f_R(x)),\, y \right) \right],$$

where $\mathcal{D}$ is the data distribution and $\mathcal{L}$ is a suitable loss function (e.g., mean squared error), the residual calibrator r learns to model the remaining variance in y that h does not capture. The linearity of r ensures that its contribution to the prediction is transparent and explainable. Each residual feature $[f_R(x)]_i$ contributes to $\hat{y}(x)$ proportionally to its corresponding weight $[w_r]_i$:

$$\frac{\partial \hat{y}(x)}{\partial [f_R(x)]_i} = [w_r]_i.$$

Similarly, for the explainable features, we have:

$$\frac{\partial \hat{y}(x)}{\partial [f_H(x)]_i} = [w_h]_i.$$

This allows us to directly understand each feature's impact on the prediction. Furthermore, during training, both h and r can update their parameters to enhance overall model performance. The orthogonality condition allows us to optimize w_h and w_r separately. Considering a convex and differentiable loss function $\ell(\hat{y}, y)$, the gradients with respect to w_h and w_r are:

$$\nabla_{w_h} \mathcal{L} = \mathbb{E}_{(x,y)} \left[\ell' \left(\hat{y}(x), y \right) f_H(x) \right], \quad \nabla_{w_r} \mathcal{L} = \mathbb{E}_{(x,y)} \left[\ell' \left(\hat{y}(x), y \right) f_R(x) \right],$$

where ℓ' denotes the derivative of ℓ with respect to its first argument. Since $f_H(x)$ and $f_R(x)$ have disjoint supports, the inner product $f_H(x)^\top f_R(x) = 0$, and thus the updates to w_h and w_r do not interfere with each other. We formalize these observations in the following theorem:

Theorem A.10. *Let $\mathcal{X}$ and $\mathcal{Y}$ be the input and output spaces, respectively. Let $f : \mathcal{X} \to \mathbb{R}^d$ be a pre-trained feature mapping, and let $h : \mathbb{R}^d \to \mathcal{Y}$ be an explainable linear model operating on the explainable features $f_H(x)$. The residual calibrator $r : \mathbb{R}^d \to \mathcal{Y}$, defined on the residual features $f_R(x)$, captures the variance not explained by h in an explainable manner, thereby preserving the overall model's explainability.*

Proof of Theorem A.10. As established, the combined model's prediction is:

$$\hat{y}(x) = h(f_H(x)) + r(f_R(x)) = w_h^\top f_H(x) + b_h + w_r^\top f_R(x) + b_r.$$

The orthogonality of $f_H(x)$ and $f_R(x)$, along with the disjoint supports of w_h and w_r, ensures that the cross terms vanish, shown as $w_h^\top f_R(x) = 0, \quad w_r^\top f_H(x) = 0$. Therefore, the combined prediction simplifies to sum of individual contributions from h and r. To understand how r captures the unexplained variance, consider the total variance of y decomposed into the variance explained by h and the residual variance:

$$\mathrm{Var}(y) = \mathrm{Var}\left(h(f_H(x))\right) + \mathrm{Var}\left(y - h(f_H(x))\right) + 2\ \mathrm{Cov}\left(h(f_H(x)),\, y - h(f_H(x))\right).$$

However, since $y - h(f_H(x))$ is uncorrelated with $h(f_H(x))$ under certain conditions, the covariance term becomes zero, leading to:

$$\mathrm{Var}(y) = \mathrm{Var}\left(h(f_H(x))\right) + \mathrm{Var}\left(y - h(f_H(x))\right).$$

The residual calibrator r models the residual $y - h(f_H(x))$, aiming to minimize $\mathrm{Var}\left(y - h(f_H(x)) - r(f_R(x))\right)$. Since r is linear and operates on $f_R(x)$, and given that $f_H(x)$ and $f_R(x)$ are orthogonal, the variance captured by $r(f_R(x))$ does not overlap with that captured by $h(f_H(x))$. This additive property ensures that the total variance explained by the combined model is:

$$\mathrm{Var}\left(h(f_H(x)) + r(f_R(x))\right) = \mathrm{Var}\left(h(f_H(x))\right) + \mathrm{Var}\left(r(f_R(x))\right),$$

due to the independence arising from orthogonality. The explainability of r is preserved because:

- **Transparency:** The linearity of r allows us to interpret the contribution of each residual feature directly through its weight in w_r.
- **Non-Interference:** Orthogonality guarantees that r does not affect the interpretability of h, as they operate on separate feature subsets.
- **Predictive Enhancement:** r enhances the predictive performance by capturing additional patterns in the data that h alone cannot explain.

Moreover, from a functional analysis perspective, the projection operators P_H and P_R associated with $f_H(x)$ and $f_R(x)$ satisfy $P_H + P_R = I_d$, where I_d is the identity matrix in $\mathbb{R}^d$. This confirms that the entire feature space is covered by the combined subspaces, and there is no loss of information in the decomposition. Furthermore, considering the operator norms of h and r:

$$\|h\|_{\text{op}} = \sup_{\|f_H(x)\|=1} |h(f_H(x))|, \quad \|r\|_{\text{op}} = \sup_{\|f_R(x)\|=1} |r(f_R(x))|,$$

we can analyze the stability and boundedness of both models. The boundedness of h and r ensures that small changes in the input features lead to proportionally small changes in the predictions, which is desirable for model robustness and interpretability. Thus, r captures the variance not explained by h in an explainable manner, preserving the overall model's explainability. This completes the proof of Theorem A.10. The final step of ***MoleX*** involves training the residual calibrator r. With the parameters of the explainable model h frozen (or updated separately due to orthogonality), the calibrator corrects mispredicted samples from h. By optimizing the objective:

$$\min_r \mathbb{E}_{(x,y)\sim\mathcal{D}}\left[\mathcal{L}\left(h(f_H(x)) + r(f_R(x)),\, y\right)\right],$$

prediction errors are iteratively fixed, progressively aligning overall predictions with target values. The design of r as a linear model and its orthogonality with h ensure that explainability is maintained while enhancing model performance. Moreover, each feature's impact on the prediction can be directly understood through the corresponding weights in w_h and w_r. Since $f_H(x)$ and $f_R(x)$ are orthogonal, and their weight vectors w_h and w_r have disjoint supports, we have:

$$\frac{\partial \hat{y}(x)}{\partial [f(x)]_i} = \begin{cases} [w_h]_i, & \text{if } i \in I_H, \\ [w_r]_i, & \text{if } i \in I_R. \end{cases}$$

This explicit form provides clear interpretability of the model's predictions, allowing practitioners to understand and trust the contributions of individual features. Thus, under the conditions of linearity and orthogonality, the residual calibrator r preserves explainability when combined with h. The combined model benefits from improved predictive accuracy while retaining transparency, satisfying both performance and interpretability objectives.

This completes the proof. □

A.6 DATASET DETAILS

We use six mutagenicity datasets and one hepatotoxicity dataset. The mutagenicity datasets are: Mutag (Debnath et al., 1991), Mutagen (Morris et al., 2020), PTC-FM (Toivonen et al., 2003), PTC-FR (Toivonen et al., 2003), PTC-MM (Toivonen et al., 2003), PTC-MR (Toivonen et al., 2003), and the hepatotoxicity dataset is the Liver (Liu et al., 2015). Followed by Morris et al. (2020), we list the summary statistics of these datasets as

Table 3: Summary statistics of seven datasets

Dataset	Mutag	Mutagen	PTC-FM	PTC-FR	PTC-MM	PTC-MR	Liver
Samples	188	4337	349	351	336	344	587
Classes	2	2	2	2	2	2	3
Ground truth	120	724	58	49	51	61	187

Note: Ground truth refers to the number of annotated samples in each dataset.

The ground truth indicates the true molecular substructures that impact molecular properties. As verified by Lin et al. (2022); Debnath et al. (1991), the ground truth substructures for six mutagenicity datasets consist of an aromatic group, such as a benzene ring, bonded with another functional group, such as methoxy, oxhydryl, nitro, or carboxyl groups (note that ground truth exists only for the mutagenic class). For the Liver dataset, the ground truth annotated by chemists are: fused tricyclic saturated hydrocarbon moiety, hydrazines, arylacetic acid, sulfonamide moiety, aniline moiety, a class of proton pump inhibitor drugs, acyclic bivalent sulfur moiety, acyclic di-aryl ketone moiety, para oxygen and nitrogen di-substituted benzene ring, a relatively small number of com- pounds in the expanded LiverTox dataset, halogen atom bonded to a sp^3 carbon, and fused tricyclic structural moiety. A detailed illustration of Liver's ground truth are provided by Liu et al. (2015).

A.7 IMPLEMENTATION DETAILS

Our model is pre-trained on all data in the ZINC dataset (over 230 million compounds) using ChemBERTa-2, with 15% (default setting) of tokens in each input randomly masked. We extract all functional groups in the ZINC dataset as the vocabulary to expand the LLM's tokenizer so that the fine-tuned LLM can better encode functional group-level inputs. We then fine-tune this model on Mutag, Mutagen, PTC-FM, PTC-FR, PTC-MM, PTC-MR, and Liver datasets. The fine-tuning is conducted on $1\times$ NVIDIA RTX3090 GPU for about 3 hours. The detailed hyperparameters with their values are given in table 4. For experiments on model performance, we employ chain-of-thought prompting for the molecular property prediction tasks on LLMs.

Hyperparameter	Value
learning rate	1e-5
batch size	128
epochs	30
weight decay	0.01
gradient clipping	1.0
warmup proportion	0.06
max sequence length	1024
optimizer	AdamW
dropout rate	0.1
gradient accumulation steps	1
mixed precision training	True

Table 4: Hyperparameters and their values we used for fine-tuning

We offer the pseudo code to explain our fine-tuning procedure as shown in algorithm 2.

Algorithm 2 Fine-tuning LLM with Group SELFIES

Input: Fine-tuning dataset $\mathcal{S}_F = \{(x_i, y_i)\}$ where x_i are Group SELFIES, y_i are molecular properties.
Input: Initialize ChemBERTa-2 model parameters θ.
Input: Prior distribution $p_0(t) = \mathcal{N}(0, I)$.
Input: Learning rate η and trade-off parameter β.

while not converged **do**
  for each mini-batch $\mathcal{B} \subset \mathcal{S}_F$ **do**
    for each $(x_i, y_i) \in \mathcal{B}$ **do**
      Compute encoder mean and covariance:

$$\mu_i = f_e^{\mu}(x_i), \quad \Sigma_i = f_e^{\Sigma}(x_i)$$

      Sample $\epsilon_i \sim \mathcal{N}(0, I)$
      Generate embedding using reparameterization trick:

$$t_i = \mu_i + \Sigma_i^{1/2} \cdot \epsilon_i$$

      Compute decoder loss:

$$\mathcal{L}_{\text{dec}}(i) = -\log q_\theta(y_i|t_i)$$

      Compute KL divergence:

$$\mathcal{L}_{\text{KL}}(i) = D_{\text{KL}}\left(p_\theta(t_i|x_i) \parallel p_0(t)\right)$$

      Compute total loss:

$$\mathcal{L}_i = \mathcal{L}_{\text{dec}}(i) + \beta \cdot \mathcal{L}_{\text{KL}}(i)$$

    Compute batch loss:

$$\mathcal{L}_{\mathcal{B}} = \frac{1}{|\mathcal{B}|} \sum_{i \in \mathcal{B}} \mathcal{L}_i$$

    Update model parameters:

$$\theta \leftarrow \theta - \eta \cdot \nabla_\theta \mathcal{L}_{\mathcal{B}}$$

A.8 Does the Residual Calibrator Improves Model Performance by training with more iterations?

We employ the training objective in 3.1 to learn a residual calibrator that iteratively corrects samples the linear model fails to predict accurately. We empirically study how training iterations influence the overall model predictions. As shown in fig. 4, we visualize the model performance on the Mutag, Mutagen, PTC-MR, and Liver datasets under different numbers of training iterations. As training iterations increase, model performance improves significantly until reaching a threshold. This suggests that more iterations on our designed loss lead to better performance. After the threshold, the model overfits the data, resulting in performance degradation. Therefore, increasing the number of training iterations helps improve model performance. Empirically, we found that 5 iterations yield optimal performance. A theoretical demonstration shows that training with multiple iterations increases model performance until a threshold, after which it declines, as follows.

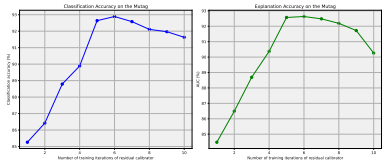

(a) Mutag

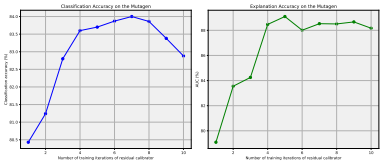

(b) Mutagen

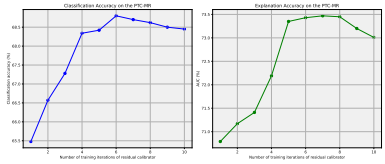

(c) PTC-MR

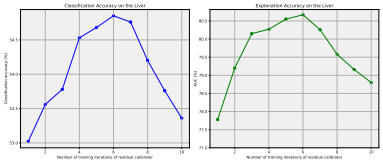

(d) Liver

Figure 4: The model performance with different training iterations of the residual calibrator

Problem Setup. Given the objective the residual calibrator minimized during training:

$$\min_{h,r} \mathbb{E}_{(x,y)\sim\mathcal{S}_{\text{train}}} \left[\mathcal{L}\left(h(f_H(x)) + r(f_R(x)),\ y\right)\right], \tag{A.12}$$

where $\mathcal{S}_{\text{train}}$ is the empirical distribution of the training data and $\mathcal{L} : \mathbb{R} \times \mathbb{R} \to \mathbb{R}_{\geq 0}$ is a convex, differentiable loss function, e.g., the squared loss $\mathcal{L}(\hat{y}, y) = \frac{1}{2}(\hat{y} - y)^2$. We demonstrate that: initially, as the residual calibrator r is trained, the model's performance on unseen data improves, i.e., the generalization loss decreases. Beyond a certain threshold, further minimization of the training loss leads to overfitting, where the generalization loss starts to increase, and prediction accuracy on unseen data degrades.

Proof. We aim to demonstrate that learning the residual calibrator r with multiple training iterations initially improves the model accuracy, but after a certain training threshold, continued minimization of the training loss leads to overfitting, leading to the predictive accuracy on unseen data decline.

Let $\mathcal{X}$ and $\mathcal{Y}$ be the input and output spaces, respectively. Consider a feature extraction function $f : \mathcal{X} \to \mathbb{R}^d$ that maps inputs to a d-dimensional feature space. We assume that f can be decomposed into two components:

$$f(x) = f_H(x) + f_R(x),$$

where $f_H(x) \in \mathbb{R}^{d_c}$ represents the explainable features used by the explainable model h, and $f_R(x) \in \mathbb{R}^{d_r}$ represents the residual features used by the residual calibrator r, with $d = d_c + d_r$. We assume that the feature components $f_H(x)$ and $f_R(x)$ are orthogonal, which means:

$$\langle f_H(x), f_R(x) \rangle = 0 \quad \text{for all } x \in \mathcal{X}.$$

The explainable model $h : \mathbb{R}^{d_c} \to \mathbb{R}$ is defined as a linear model:

$$h(f_H(x)) = W_h^\top f_H(x) + b_h,$$

where $W_h \in \mathbb{R}^{d_c}$ and $b_h \in \mathbb{R}$ are the weights and bias of h. The residual calibrator $r : \mathbb{R}^{d_r} \to \mathbb{R}$ is also defined as a linear model:

$$r(f_R(x)) = W_r^\top f_R(x) + b_r,$$

where $W_r \in \mathbb{R}^{d_r}$ and $b_r \in \mathbb{R}$ are the weights and bias of r. Due to the orthogonality of $f_H(x)$ and $f_R(x)$, the overall prediction model becomes:

$$\hat{y}(x) = h(f_H(x)) + r(f_R(x)) = W_h^\top f_H(x) + W_r^\top f_R(x) + b_h + b_r.$$

Our objective is to minimize the expected loss:

$$\mathcal{L}(W_h, W_r, b_h, b_r) = \mathbb{E}_{(x,y)\sim\mathcal{D}} \left[\ell \left(\hat{y}(x), y \right) \right],$$

where $\ell \left(\hat{y}(x), y \right)$ is a convex and differentiable loss function, such as the squared loss $\ell(\hat{y}, y) = \frac{1}{2}(\hat{y} - y)^2$, and $\mathcal{D}$ is the data distribution. We begin by considering the training loss over a finite training dataset $\{(x_i, y_i)\}_{i=1}^n$:

$$\mathcal{L}_{\text{train}}(W_h, W_r, b_h, b_r) = \frac{1}{n} \sum_{i=1}^{n} \ell \left(\hat{y}(x_i), y_i \right).$$

Initially, when r is untrained or minimally trained, the model may be underfitting, and both the training loss $\mathcal{L}_{\text{train}}$ and generalization loss $\mathcal{L}_{\text{gen}}$ are high. By updating W_r and b_r via gradient descent to minimize $\mathcal{L}_{\text{train}}$, we have the updates:

$$W_r^{(t+1)} = W_r^{(t)} - \eta \nabla_{W_r} \mathcal{L}_{\text{train}}(W_h, W_r^{(t)}, b_h, b_r^{(t)}),$$

$$b_r^{(t+1)} = b_r^{(t)} - \eta \nabla_{b_r} \mathcal{L}_{\text{train}}(W_h, W_r^{(t)}, b_h, b_r^{(t)}),$$

where $\eta > 0$ is the learning rate, and t denotes the iteration number. Since ℓ is convex and differentiable, these updates ensure that the training loss decreases:

$$\mathcal{L}_{\text{train}}^{(t+1)} \leq \mathcal{L}_{\text{train}}^{(t)}.$$

During this phase, r captures genuine patterns in the residual features $f_R(x)$ that are not explained by h. Consequently, the generalization loss decreases as well:

$$\mathcal{L}_{\text{gen}}^{(t+1)} \leq \mathcal{L}_{\text{gen}}^{(t)},$$

where $\mathcal{L}_{\text{gen}}(W_h, W_r, b_h, b_r) = \mathbb{E}_{(x,y)\sim\mathcal{D}} \left[\ell \left(\hat{y}(x), y \right) \right]$.

However, as training continues, W_r and b_r may begin to fit the noise or idiosyncrasies specific to the training data, especially if the model has a high capacity (i.e., d_r is large relative to n). The fitting capacity of r allows it to minimize $\mathcal{L}_{\text{train}}$ further, but this comes at the cost of increasing complexity.

To formalize this, we consider the concept of Rademacher complexity $\mathfrak{R}_n(\mathcal{H})$ for the hypothesis class $\mathcal{H}$ associated with r. The Rademacher complexity provides a measure of the model's ability to fit random noise in the data. The generalization error can be bounded as:

$$\mathcal{L}_{\text{gen}}(W_h, W_r, b_h, b_r) \leq \mathcal{L}_{\text{train}}(W_h, W_r, b_h, b_r) + 2\mathfrak{R}_n(\mathcal{H}) + \delta,$$

where δ is a constant dependent on the loss function and confidence level. As $\|W_r\|$ increases due to continued training, $\mathfrak{R}_n(\mathcal{H})$ increases, reflecting the higher complexity of r. This leads to circumstances that:

$$\mathcal{L}_{\text{train}}^{(t+1)} < \mathcal{L}_{\text{train}}^{(t)} \quad \text{but} \quad \mathcal{L}_{\text{gen}}^{(t+1)} > \mathcal{L}_{\text{gen}}^{(t)} \quad \text{for } t \geq t^*,$$

where t^* is the iteration threshold beyond which overfitting occurs.

For linear models, the Rademacher complexity can be bounded by:

$$\mathfrak{R}_n(\mathcal{H}) \leq \frac{B\|W_r\|}{\sqrt{n}},$$

where $B = \sup_{x \in \mathcal{X}} \|f_R(x)\|$. As $\|W_r\|$ increases, $\mathfrak{R}_n(\mathcal{H})$ increases, leading to a wider generalization gap. This increase in model complexity without a corresponding increase in true predictive power causes the model to generalize poorly on unseen data, despite the training loss decreasing. This phenomenon is a bias-variance trade-off: the variance increases significantly due to overfitting, outweighing any small reductions in bias achieved by further minimizing the training loss.

In conclusion, while initial training of the residual calibrator r improves model accuracy by reducing both the training loss and the generalization loss, continued training beyond a certain threshold leads to overfitting. The residual calibrator begins to model noise in the training data, increasing its complexity and causing the generalization loss to increase. This results in a decline in prediction accuracy on unseen data, suggesting the importance of strategies such as early stopping or regularization to prevent overfitting.

This completes the proof. □

A.9 How to choose the optimal number of principal components?

To empirically determine the optimal number of principal components for our implementation, we compare model performance metrics (classification accuracy and explanation accuracy) across four datasets under different numbers of principal components. As shown in fig. 5, both metrics tend to converge as the number of principal components exceeds 20. This indicates that when the number of components surpasses 20, the contribution of additional components to molecular property prediction becomes trivial. In this scenario, adding more components produces diminishing marginal benefits while significantly increasing model complexity, which in turn reduces explainability. Therefore, we choose the top 20 principal components to explain the variance in molecular properties, seeking for a balance between performance and explainability.

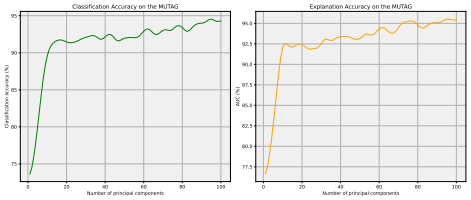

(a) Mutag

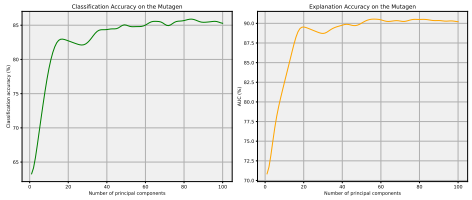

(b) Mutagen

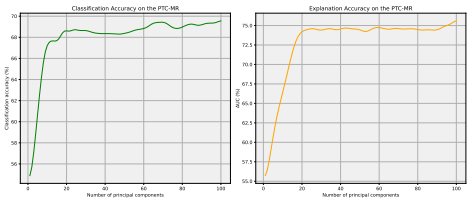

(c) PTC-MR

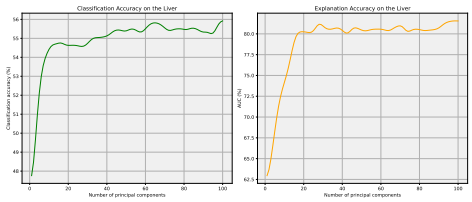

(d) Liver

Figure 5: Optimal number of principal components

A.10 DOES EFPCA EFFECTIVELY WORKS?

In addition to the analysis in appendix A.9, we demonstrate that the dimensionality reduction by EFPCA effectively preserves the most explanatory components. We compare the model performance across seven datasets *with and without dimensionality reduction*. As shown in table 5, when using only 20 PCs, the model performance improves by no more than 5% compared to using all 384 components (i.e., no dimensionality reduction). This indicates that EFPCA effectively preserves the most task-relevant and important information in LLM embeddings while excluding noisy components. These preserved components achieve comparable performance to the models with all components while being significantly simpler and more explainable. This showcases the success of our dimensionality reduction in maintaining model performance while enhancing explainability.

Dataset	Classification Accuracy (%)	Explanation Accuracy (%)
Mutag	94.9±1.6	96.1±3.0
Mutagen	86.4±1.4	91.2±1.6
PTC-FR	78.7±1.2	82.7±1.7
PTC-FM	68.1±1.5	81.1±2.0
PTC-MR	70.5±1.7	76.5±2.6
PTC-MM	80.9±2.7	75.3±2.2
Liver	57.3±1.6	83.8±1.9

Table 5: Model performance *without* EFPCA over seven datasets

A.11 DOES THE CHOICE OF n IN N-GRAM MAKES A DIFFERENCE?

We compare the different values of n in n-gram via cross-validation based on our two evaluation metrics, classification accuracy and explanation accuracy. The results in fig. 6 suggest an overall trend that as n goes from 1 to 3, both classification accuracy and explanation accuracy improve; as n goes from 4 to 9, both classification accuracy and explanation accuracy drop. On the four datasets we used for experiments, three of them show that good model performance can be achieved when n is taken to be 3. As n grows from small to large, it encourages the model to capture more contextual semantics, including interactions between functional groups, which allows for a significant improvement in prediction. When n exceeds a certain threshold, irrelevant or even toxic information emerges from the captured contextual information (i.e., irrelevant long-range dependencies), making the overall model utility gradually decreases.

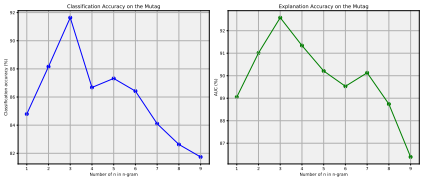

(a) Mutag

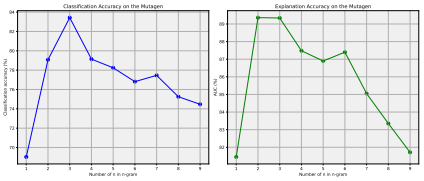

(b) Mutagen

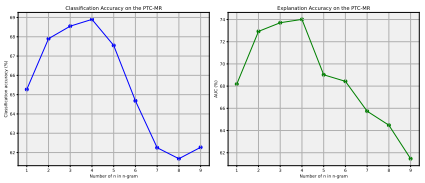

(c) PTC-MR

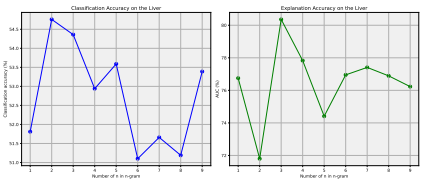

(d) Liver

Figure 6: The choice of n in n-gram on the Mutag, Mutagen, PTC-MR, and Liver datasets

A.12 MORE EXPLANATION VISUALIZATIONS

We randomly select one sample from each of the six remaining datasets and provide explanation visualizations based on *MoleX*. Specifically, fig. 7, fig. 8, fig. 9, fig. 10, fig. 11, and fig. 12 display the samples selected from the Mutagen, PTC-FM, PTC-MM, PTC-FR, PTC-MR, and Liver datasets, respectively. On the left, we compare molecular substructures identified by different methods, with ground truth showing expert-validated substructures influencing molecular properties. Red marks on the molecular graph highlight key components identified by each method. We compare with three baselines: OrphicX (Lin et al., 2022), GNNExplainer (Ying et al., 2019), and PGExplainer (Luo et al., 2020), as well as *MoleX* with and without residual calibration (w/ denotes *with* and w/o denotes *without*). On the right, we show *MoleX*'s n-gram contribution scores (0–100) for functional groups, with higher scores indicating greater influence on molecular properties.

Taking fig. 7 as an example, *MoleX* precisely identifies the ground truth substructures for the sample from the Mutagen dataset. Specifically, *MoleX* highlights the benzene ring bonded with an amino group on the upper left as vital substructures to explain the molecule's mutagenicity. The contribution scores computed by *MoleX* indicate that the benzene ring has the highest contribution to molecular properties, followed by the amino group. This aligns with the ground truth that a benzene ring bonded with an amino group leads to mutagenicity (Lin et al., 2022; Debnath et al., 1991). Therefore, *MoleX* accurately captures the important functional groups (i.e., the benzene ring and the amino group) and the interaction between them, revealing their precise bonding. As the ground truth indicates, only the bonded benzene and amino group together impact the molecular properties. In contrast, other methods provide only atom or bond-level explanations and fail to discover important functional groups as a whole. They identify only a few atoms and bonds in the benzene or amino group and fail to capture the interaction between these two functional groups. Consequently, these atom or bond-level explanations are insufficiently faithful in explaining molecular properties, as individual atoms or bonds have limited impact on overall molecular properties (Mirghaffari et al., 2021). The explanation visualizations for samples from other datasets also demonstrate *MoleX*'s effectiveness in identifying important substructures and their interactions, aligning with chemical concepts to explain molecular property predictions.

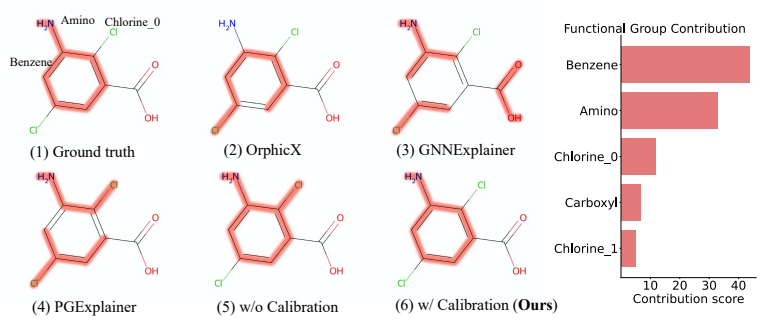

Figure 7: Explanation visualization of a molecule from the Mutagen dataset (left), and contribution scores of the identified functional groups offered by *MoleX* (right).

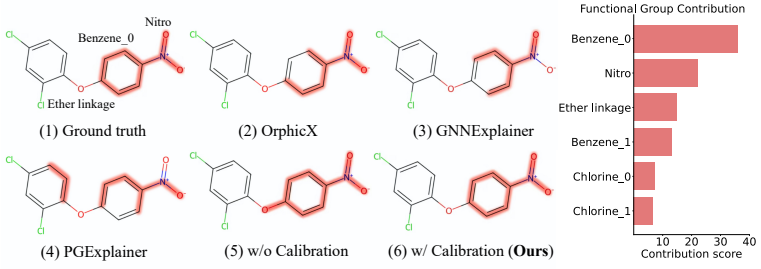

Figure 8: Explanation visualization of a molecule from the PTC-FM dataset (left), and contribution scores of the identified functional groups offered by *MoleX* (right).

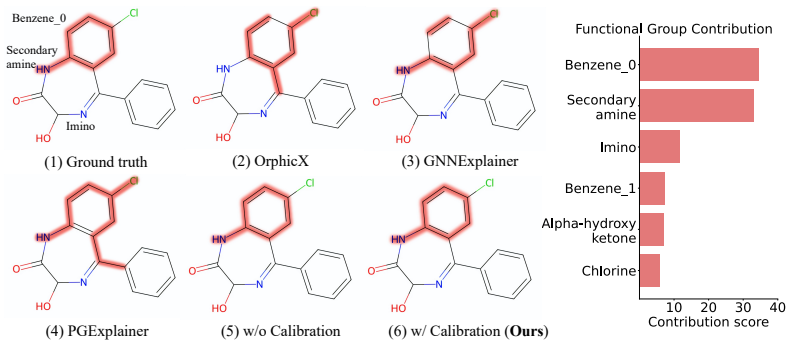

Figure 9: Explanation visualization of a molecule from the PTC-MM dataset (left), and contribution scores of the identified functional groups offered by *MoleX* (right).

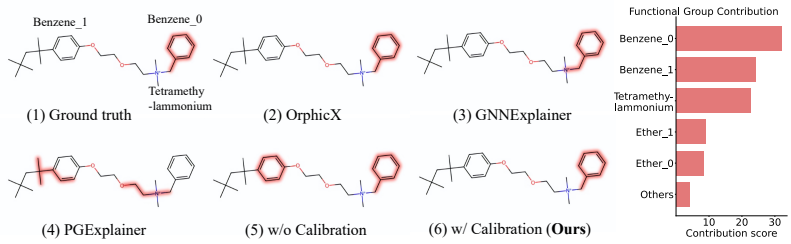

Figure 10: Explanation visualization of a molecule from the PTC-FR dataset (left), and contribution scores of the identified functional groups offered by *MoleX* (right).

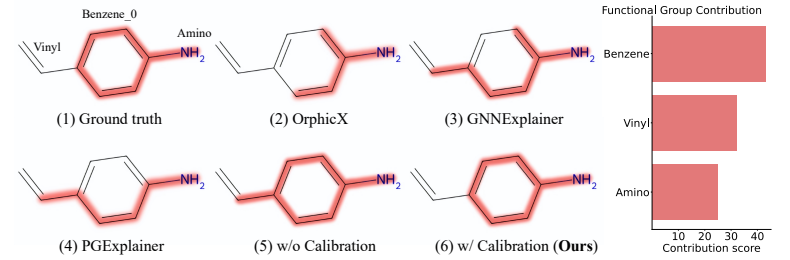

Figure 11: Explanation visualization of a molecule from the PTC-MR dataset (left), and contribution scores of the identified functional groups offered by *MoleX* (right).

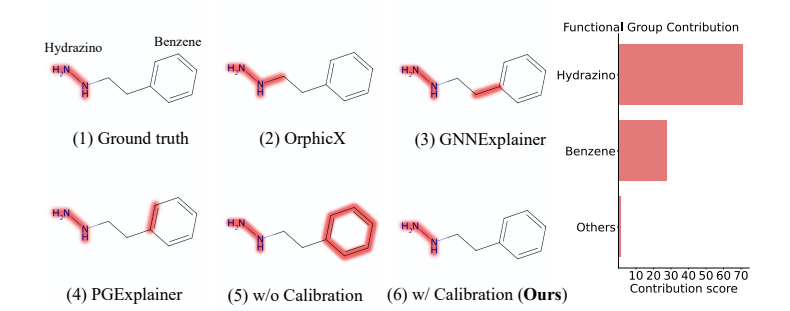

Figure 12: Explanation visualization of a molecule from the Liver dataset (left), and contribution scores of the identified functional groups offered by *MoleX* (right).

A.13 CAN OTHER STATISTICAL LEARNING MODELS BE AUGMENTED WITH THE LLM KNOWLEDGE?

In addition to the linear model, we augment various statistical learning models with the LLM knowledge and test them on seven datasets. The classification accuracy and explanation accuracy are shown in table 6 and table 7, respectively. Other linear models, such as ridge regression, LASSO, and linear discriminant analysis, achieve comparable performance to *MoleX* and showcase the generalizability of LLM knowledge augmentation on linear models. Additionally, the polynomial regression, as a more complicated linear model, achieves better performance compared to the simpler ones shown above. For more complex models, such as tree-based and ensemble learning models, the performance is even better, achieving incredible results across all seven datasets. These empirical studies suggest that augmenting statistical machine learning models with LLM knowledge significantly improves performance. Moreover, compared to simple models, the models exhibit more powerful data fitting capabilities become more predictive after the LLM augmentation. However, model complexity generally trades off with explainability. Considering this, we select the logistic regression as our base model due to its optimal balance between explainability and performance.

Table 6: Classification Accuracy across different machine learning models over seven datasets (%)

Method	Mutag	Mutagen	PTC-FR	PTC-FM	PTC-MR	PTC-MM	Liver
Ridge Regression	90.7±1.2	84.1±1.3	72.4±2.0	65.2±2.0	69.8±1.4	77.5±1.5	58.1±1.6
LASSO	91.9±1.7	84.4±0.7	75.1±2.1	65.8±1.7	65.2±0.9	74.2±1.2	58.7±1.8
Linear Discriminant Analysis	89.9±1.9	83.6±1.2	75.2±1.9	65.7±1.9	69.3±1.8	76.8±2.0	57.7±1.3
Polynomial Regression	93.9±2.4	87.2±2.0	77.1±2.1	67.3±1.8	70.2±2.3	79.5±1.8	60.2±2.4
Support Vector Machine	93.9±1.6	86.6±1.5	73.4±1.9	69.3±2.6	69.5±2.0	78.6±1.3	61.5±2.9
Decision Tree	89.7±2.1	79.5±1.2	72.4±1.8	64.3±2.1	68.5±1.5	74.4±1.4	59.5±2.2
Random Forest	92.8±2.7	84.4±1.7	77.3±2.1	68.6±2.5	71.0±2.2	77.2±2.1	62.7±2.7
Gradient Boosting Machine	94.8±2.1	85.3±1.9	78.9±1.9	69.4±2.8	72.2±2.1	79.2±1.9	63.9±2.6
XGBoost	94.6±2.3	85.0±2.0	78.7±2.2	70.1±2.3	73.4±2.9	78.1±2.1	63.0±2.3
MoleX (Ours)	91.6±2.0	83.7±0.9	74.4±1.9	64.2±1.4	68.4±2.3	76.4±1.8	54.9±2.4

Table 7: Explanation Accuracy across different machine learning models over seven datasets (%)

Method	Mutag	Mutagen	PTC-FR	PTC-FM	PTC-MR	PTC-MM	Liver
Ridge Regression	92.8±1.1	89.5±1.3	79.0±1.2	78.1±1.6	72.5±2.5	69.7±2.3	82.4±1.7
LASSO	92.3±1.5	89.6±0.9	76.9±1.8	81.2±1.9	70.4±2.3	70.7±2.1	81.3±1.8
Linear Discriminant Analysis	92.9±1.8	88.5±1.9	80.7±2.3	80.1±2.2	71.7±2.8	71.3±1.6	87.8±1.6
Polynomial Regression	94.3±2.1	91.9±1.6	80.1±1.9	82.9±1.9	79.3±2.3	75.4±1.7	81.0±2.2
Support Vector Machine	92.0±1.7	92.0±1.6	84.7±2.2	86.3±2.0	80.1±2.3	76.0±2.3	81.9±2.1
Decision Tree	87.6±1.9	89.1±1.5	78.6±2.0	80.7±1.6	73.1±2.1	74.2±1.8	76.0±1.8
Random Forest	93.2±1.9	90.5±1.8	82.1±2.1	84.2±2.2	74.2±2.0	74.5±2.1	81.2±2.0
Gradient Boosting Machine	92.7±2.2	92.4±1.5	82.9±2.3	85.2±2.4	73.9±2.9	77.7±2.6	84.5±2.4
XGBoost	95.6±1.8	90.7±1.7	84.0±2.2	82.0±2.3	74.4±2.7	77.4±2.2	86.2±2.5
MoleX (Ours)	92.6±1.7	89.0±0.9	79.3±2.6	77.9±2.6	73.4±2.8	72.3±3.0	80.3±2.5

A.14 CLASSIFICATION ANALYSIS VIA CONFUSION MATRIX

As shown in fig. 13, we visualize the classification result via confusion matrix at a random round on the Mutag and PTC-MR datasets. For Mutag, we achieve high precision in predicting the positive class due to fewer false positives and high recall for the positive class, reflecting the model's effectiveness in identifying positive instances. Furthermore, the model shows a good balance between precision and recall, with a low number of false positives and false negatives. For PTC-MR, the model achieves lower precision compared to the Mutag due to a higher number of false positives. The confusion matrix also suggests that the model struggles with false negatives and false positives, indicating areas for improvement. This analysis highlights the strengths and weaknesses of the model, providing insight for further model refinement.

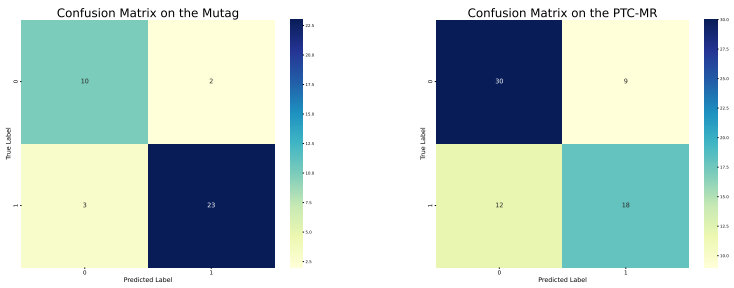

(a) Mutag (b) PTC-MR

Figure 13: The confusion matrix of classification results on the Mutag and PTC-MR datasets

Table 8: Classification accuracy over three datasets (%). The best results are highlighted in **bold**.

Methods	BBBP	ClinTox	HIV
GCN (Kipf and Welling, 2016)	78.5±0.8	78.2±1.0	72.1±0.8
DGCNN (Zhang et al., 2018)	80.0±0.9	79.0±1.1	73.2±1.4
edGNN (Jaume et al., 2019)	79.0±0.9	77.5±1.0	69.5±0.7
GIN (Xu et al., 2018)	82.0±0.7	80.9±0.9	74.0±1.3
RW-GNN (Nikolentzos and Vazirgiannis, 2020)	81.0±1.0	78.5±1.0	75.5±0.4
DropGNN (Papp et al., 2021)	83.0±0.9	81.0±0.8	64.5±0.6
IEGN (Maron et al., 2018)	85.5±1.0	80.1±0.5	76.0±0.9
LLAMA3.1-8b (Dubey et al., 2024)	69.0±2.5	52.0±2.7	56.0±1.5
GPT-4o (Achiam et al., 2023)	74.5±2.3	56.4±2.5	64.5±1.8
ChemBERTa-2 (Ahmad et al., 2022)	78.0±1.5	71.5±1.4	73.0±0.6
Logistic Regression	66.5±0.8	60.2±0.6	60.1±0.7
Decision Tree (Quinlan, 1986)	70.3±0.8	62.8±0.6	66.2±0.8
Random Forest (Breiman, 2001)	73.5±0.9	68.5±0.7	69.8±1.9
XGBoost (Chen and Guestrin, 2016)	74.2±0.8	67.8±0.8	70.2±1.2
w/o Calibration	80.6±1.3	85.9±0.7	75.6±1.3
w/ Calibration (Ours)	**93.1±0.6**	**94.1±0.8**	**81.3±1.4**

A.15 An illustration of Group SELFIES

As illustrated in fig. 14, the 4-Nitroanisole ($C_7H_7NO_3$) can be represented by Group SELFIES with three functional groups separated by square brackets: a benzene ring, a nitro group, and a methoxy group (different functional groups are displayed in different colors).

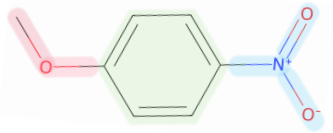

SMILES: C1=CC(=C(C=C1N)C(=O)O)O

Group SELFIES: [:0benzene][Ring2]
[:0methoxy][pop][Branch][:1nitro][pop]

Figure 14: Molecular representation of 4-Nitroanisole ($C_7H_7NO_3$)

A.16 More empirical evaluation on the robustness of *MoleX*

As the molecular data is diverse, complex, and intrinsically noisy, we offer experiments on another three datasets, covering more extensive domains/tasks in molecular property prediction to demonstrate *MoleX*'s robustness. *MoleX* performs consistently excellent across all datasets and baselines, showcasing its effective generalizability. The results of classification and explanation accuracy are shown in table 8 and table 9, respectively.

Table 9: Explanation accuracy over three datasets (%). The best results are highlighted in **bold**.

Methods	BBBP	ClinTox	HIV
GCN (Kipf and Welling, 2016)	75.1±0.4	74.6±0.6	67.6±0.6
DGCNN (Zhang et al., 2018)	77.6±1.1	79.2±0.5	73.8±1.1
edGNN (Jaume et al., 2019)	78.9±0.2	74.8±0.2	71.6±0.6
GIN (Xu et al., 2018)	80.4±0.7	77.1±0.8	70.3±0.8
RW-GNN (Nikolentzos and Vazirgiannis, 2020)	79.5±0.4	69.4±0.6	69.5±0.7
DropGNN (Papp et al., 2021)	72.6±0.6	76.7±0.2	74.4±0.3
IEGN (Maron et al., 2018)	80.8±0.7	79.1±0.4	69.5±1.2
Logistic Regression	67.9±0.3	61.9±0.2	61.8±0.6
Decision Tree (Quinlan, 1986)	68.4±1.5	66.8±0.8	64.0±1.2
Random Forest (Breiman, 2001)	73.3±1.1	68.3±1.7	65.7±1.3
XGBoost (Chen and Guestrin, 2016)	73.5±1.4	65.5±1.6	67.8±0.9
w/o Calibration	81.1±1.8	78.6±1.5	71.2±1.1
w/ Calibration (Ours)	**90.8±1.6**	**92.8±1.9**	**82.4±1.2**

A.17 Broader Impact

This study on explainable molecular property prediction using an LLM-augmented linear model offers significant real-world applications. The efficiency of linear models enables fast inference on large-scale molecular data, potentially accelerating drug discovery and materials design. Enhanced by LLM-derived features, our method combines predictive accuracy, cost-effectiveness, and computational efficiency, addressing critical needs in fields like healthcare and materials science. Its high explanation accuracy provides faithful insights into structure-property relationships, fostering adoption in high-stakes domains and supporting scientific discovery. Additionally, this balance of accuracy, explainability, and efficiency serves as a template for developing trustworthy AI in other fields, with potential impacts on personalized medicine and sustainable chemistry. However, responsible implementation is crucial to mitigate risks, such as over-reliance on predictions or misuse in harmful molecule design, emphasizing the need for expert validation and research into limitations.

A.18 Limitations and future works

The proposed explainable molecular property prediction method has some limitations and needs further studies.

- **Generalizability:** Enhancing the generalizability of explainable models to deal with different molecular datasets across various chemical domains while preserving explainability to structure-property relationships remains a persistent challenge.
- **Impact of LLM choices:** Though our empirical studies discuss the model performance of Llama3.1 and GPT-4o on molecular property prediction, LLM quality is still a topic that deserves to be explored in-depth. Future studies may discuss how LLM choices impact the augmented linear model, e.g., model performance change using weak LLMs or LLMs without fine-tuning.
- **Trade-off between complexity and performance:** In pursuit of explainability, we employ a linear model, which inherently risks underfitting when faced with complex data patterns. Our preliminary experiments comparing *MoleX* with more sophisticated statistical learning models show marginally better performance from these complex models. Future research could explore the trade-off between model complexity and performance in the context of LLM knowledge augmentation and investigate optimal balances between explainability and performance.